International Journal of Heat and Mass Transfer 258 (2026) 128316

Contents lists available at ScienceDirect

International Journal of Heat and Mass Transfer

journal homepage: www.elsevier.com/locate/ijhmt

Computational investigation of flow condensation data from international space station microgravity and earth gravity experiments

Hyun Sung Hwang, Sunjae Kim, Steven Darges, Issam Mudawar *

Purdue University Boiling and Two-Phase Flow Laboratory (PU-BTPFL), School of Mechanical Engineering, Purdue University, 1500 Kepner Drive, Lafayette, IN 47905, USA

ARTICLE INFO

Keywords:
Computational fluid dynamics
Flow condensation
Earth gravity
Microgravity
International space station

ABSTRACT

This study validates and applies a computational modeling framework for filmwise flow condensation of n-perfluorohexane (nPFH) as part of the recently conducted Flow Boiling and Condensation Experiment (FBCE) onboard the International Space Station (ISS). The proposed model is based on the Volume of Fluid (VOF) method augmented by an additional momentum source term representing interfacial shear, which improves the model's predictive accuracy. Simulations were performed for six operating conditions, three under Earth gravity in vertical downflow orientation and three under microgravity. The model was extensively validated through comparison of predicted and experimentally measured streamwise wall temperature profiles, showing good agreement with maximum deviations of 5.1 K and 5.7 K for Earth gravity and microgravity, respectively. Following validation, the framework was employed to resolve key thermohydraulic parameters, including wall heat flux, interfacial distributions, and turbulence characteristics, thereby providing deeper insight into two-phase condensation heat transfer mechanisms and microgravity effects. These results underscore the practical utility of the developed CFD model for simulating two-phase flow condensation in both terrestrial and space thermal management systems.

1. Introduction

1.1. Two-phase flow and heat transfer in future space applications

Two-phase systems are attractive for various applications relevant to the space industry including spacecraft avionics thermal management, electronics cooling, cryogenic fuel management, planetary habitat control, and Rankine power cycles [1]. In a closed two-phase loop, the method in which the working fluid absorbs heat by boiling is highly customizable, each with its own advantages and disadvantages. Capillary flows [2], such as heat pipes, have low power requirements but are limited to relatively low heat loads. Pool boiling [3], while simple, is plagued by low critical heat flux as vapor accumulates near the surface. Falling-films [4] take advantage of body force in Earth gravity, but are inoperable in microgravity. Spray cooling [5], is suitable for dissipating high heat fluxes with uniform surface temperatures by dispersing droplets over the heated surface. Hence, spray cooling is present in several space applications such as cryogenic fuel delivery and chill down. Jet impingement [6] replicates the high heat flux capability of spray, albeit with higher pumping requirements to achieve isothermal surfaces with multiple jets. Flow boiling [7,8] is advantageous due to its reliance on fluid motion to flush bubbles away from and rewet heated surfaces, making it a prime contender for high heat flux thermal management in microgravity. However micro-channel flow boiling [9] should be employed with caution due to greater confinement effects and therefore high pressure drop in microgravity. Hybrid cooling schemes [10,11] employ two or more of the aforementioned configurations in tandem to maximize cooling potential.

Every closed two-phase loop depends on condensation to reject heat from the working fluid and return it to the liquid phase. The condenser components of such loops are typically much larger than the evaporator, owing to the relatively low heat transfer coefficients and heat fluxes associated with condensation [12]. Consequently, accurate predictive and design tools are essential for minimizing condenser size and overall system footprint.

1.2. Flow condensation in microgravity

Typically, condenser design tools are developed and validated using data obtained under Earth gravity, introducing uncertainty when applying them to microgravity environments. To ensure their reliability,

* Corresponding author.
E-mail address: mudawar@ecn.purdue.edu (I. Mudawar).

https://doi.org/10.1016/j.ijheatmasstransfer.2025.128316
Received 19 October 2025; Received in revised form 4 December 2025; Accepted 26 December 2025
Available online 30 December 2025

Nomenclature

A_c	channel cross-sectional area, [mm^2]
D	diameter, [mm]
D_h	hydraulic diameter, [mm]
E	energy per unit mass, [J/kg]
f	friction factor
G	mass velocity, [$kg/m^2.s$]
g	gravitational acceleration, [m/s^2]
g_e	gravitational acceleration on Earth, [m/s^2]
μg_e	microgravity, [m/s^2]
h_{fg}	latent heat of vaporization, [J/kg]
k_{eff}	effective thermal conductivity [W/m.K]
L	length, [mm]
$\dot{m}$	mass transfer rate, [kg/s]
P	pressure, [kPa]
$P_{f,b}$	Interfacial perimeter, [m]
q''	heat flux, [W/m^2]
Re	Reynolds number, $[GD/\mu]$
r_i	mass transfer intensity factor, [1/s]
S_E	energy source by phase change, [J/m^3]
S_M	force per unit volume, [N/m^3]
T	temperature, [K]
t	time, [s]
T_w	wall temperature, [K]
u	velocity, [m/s]
x_e	thermodynamic equilibrium quality
z	flow direction coordinate, [mm]

Greek symbols

α	void fraction
Γ	condensation rate per unit length, [kg/s.m]
κ	curvature
μ	dynamic viscosity, [kg/m-s]
ρ	density, [kg/m^3]
σ	surface tension, [N/m]
τ	shear stress, [N/m^2]

Subscripts

c	capillary
exp	experimental
f	liquid phase
fg	evaporation
g	vapor phase
gf	condensation
i	interface
in	inlet
pred	predicted
sat	saturation
SH	superheat
w	water

Acronyms

BHM	Bulk Heater Module
CFD	Computational Fluid Dynamics
CM-HT	Condensation Module for Heat Transfer
CSF	Continuous Surface Force
FBCE	Flow Boiling and Condensation Experiment
ISS	International Space Station
ITCS	ISS Thermal Control System
NASA	National Aeronautics and Space Administration
nPFH	n-Perfluorohexane
PU-BTPFL	Purdue University Boiling and Two-Phase Flow Laboratory
RTD	Resistance Temperature Detector
SST	Shear Stress Transport
UDF	User-Defined Function
VOF	Volume of Fluid

a dedicated microgravity condensation database is needed to validate existing correlations and computational models before they are used to guide the design of two-phase systems in space. However, such data remain scarce in the literature, motivating several researchers to perform condensation experiments during short-duration microgravity conditions achieved through parabolic flight campaigns.

Several researchers have investigated flow condensation under both microgravity (μg_e) and normal Earth gravity (1 g_e) conditions. In general, lower heat transfer coefficients have been reported in μg_e, primarily due to the formation of a thicker, more axisymmetric condensate film in the absence of body forces. This effect is particularly pronounced at low flow rates, as demonstrated by Berto et al. [13], who observed a 77 % reduction in heat transfer coefficient at a mass velocity of 30 kg/m^2 s. At higher flow rates, however, interfacial shear and inertial forces become dominant, mitigating gravitational effects and resulting in negligible differences between μg_e and 1 g_e performance.

However, conducting condensation experiments in microgravity using parabolic flights presents several inherent limitations. The parabolic maneuvers that generate the microgravity environment introduce small fluctuations in gravitational acceleration (known as g-jitter [14]) which can compromise the quality of the microgravity conditions. Moreover, each parabola provides only about 20 s of microgravity, often insufficient for condensation processes to reach steady state. This limitation was evident in the work of Reinarts et al. [15], where steady-state conditions were approached near the end of each parabola but could not be fully achieved.

To overcome these limitations, Mudawar et al. [16] recently performed long-duration microgravity flow condensation experiments onboard the International Space Station (ISS) as part of the Flow Boiling and Condensation Experiment (FBCE). Over a broad range of operating conditions, the resulting microgravity two-phase heat transfer coefficient dataset exhibited close agreement with corresponding terrestrial gravity measurements for both horizontal and vertical-downward flow orientations. These findings indicate that, under the tested conditions, flow inertia was sufficient to make condensation heat transfer largely insensitive to gravitational effects.

1.3. Computational studies of flow condensation

Computational Fluid Dynamics (CFD) has become a standard and reliable tool for predicting fluid behavior and heat transfer in single-phase flow. However, its application to two-phase flow, especially when phase change is involved, remains considerably less mature and robust [17]. A comprehensive review by Kharangate and Mudawar [18] attributes these limitations to the steep computational costs, lengthy simulation times, and the need to restrict analyses to relatively simple geometries. To improve the efficiency and predictive capability of two-phase CFD, researchers have focused on optimizing numerical methodologies and developing advanced sub-models that better capture the complex interfacial transport phenomena governing boiling and condensation.

One approach to improving two-phase CFD prediction accuracy is to augment the governing conservation equations with additional source terms that account for unresolved physical phenomena. Malgarinos et al. [19] introduced a ‘wetting force model’ that incorporated an additional capillary adhesion force acting at the contact line of a liquid droplet

impinging on a solid surface. Their simulations successfully predicted the maximum droplet spreading within 15 % of experimental measurements. To reduce computational cost, Xue et al. [20] modeled two-phase flow through a microchannel heat sink by treating the domain as a porous medium, with the porosity defined as the ratio of the channel width to the total pitch (channel plus wall). Momentum source terms representing viscous resistance and capillary forces were incorporated to capture the effects of the porous structure. Their model showed excellent agreement with experimental measurements of the capillary-driven suction distance across heat sinks with varying aspect ratios.

In studies involving phase change, Lee et al. [21] enhanced bubble dynamics during flow boiling by introducing a 'shear lift force' as an additional momentum source term to promote bubble departure. Incorporating this force helped preserve bubbly flow within the channel and prevented premature transition to film boiling. In a subsequent study, Lee et al. [22] introduced a 'bubble collision dispersion force' to model physical interactions between bubbles and suppress excessive coalescence within the channel. These efforts were further extended through the combined implementation of shear lift, bubble collision dispersion, and drag forces—the latter applying an additional drag on vapor bubbles moving slower than the bulk liquid—to accurately simulate flow boiling under microgravity conditions. The improved framework was successfully applied to both highly subcooled [23] and near-saturated [24] flow boiling, with results validated against long-duration, steady-state microgravity data collected onboard the ISS as part of the Flow Boiling and Condensation Experiment (FBCE) [24].

Numerous researchers have developed and reported computational methodologies for simulating condensation using CFD. Such simulations enable detailed visualization of condensate film evolution, spatial distributions of velocity and temperature, and prediction of local and overall heat transfer performance within tubes and channels. A summary of representative studies including their geometries, simulated operating conditions, and the key physical models and parameters employed is presented in Table 1.

Da Riva and Del Col [25,26] numerically investigated condensation of R134a in an isothermal circular tube under horizontal, vertical-downward, and microgravity conditions. For horizontal flow at a mass velocity of $G = 100$ kg/m^2 s, the liquid film was initially circumferentially uniform near the tube inlet but progressively accumulated along the bottom of the tube downstream as vapor quality decreased. This film nonuniformity led to approximately 62 % of the total heat transfer occurring along the upper half of the tube. Interestingly, the resulting asymmetric film distribution enhanced the overall heat transfer coefficient compared to vertical downflow. In contrast, the absence of buoyancy under microgravity produced the thickest condensate film and correspondingly the lowest heat transfer coefficients. At higher mass velocity of G = 800 kg/m^2 s, where shear forces dominate, the discrepancies among the different gravity conditions were largely mitigated.

Chen et al. [27] simulated condensation of saturated vapor FC-72 in a square channel subjected to a uniform cooling heat flux applied to three walls. The predicted sequence of flow pattern transitions, from smooth annular to wavy annular, transition, slug, bubbly, and finally single-phase liquid, showed good agreement with experimental observations. As the vapor progressed along the channel, condensation caused a reduction in vapor velocity; however, the vapor phase consistently maintained a higher velocity than the adjacent liquid phase.

Qiu et al. [28] numerically investigated the temperature and velocity fields during vertical upflow condensation of steam inside an isothermal pipe with an inner diameter of D = 12 mm. In the bubble flow regime, straight and uniform streamlines were observed, resembling those of single-phase flow. However, a large radial temperature gradient developed, resulting in significantly higher heat transfer compared to single-phase conditions. In the slug-flow regime, the streamlines were disturbed by large vapor bubbles, and buoyancy induced backflow

Table 1
Summary of previous computational studies of flow condensation.

Authors	Geometry and operating conditions	Key models and parameters
Da Riva & Del Col (2011) [25]	• R134a • Horizontal, vertical downflow, microgravity • Circular channel with $D = 1$ mm and $L = 75 – 150$ mm • $G = 100 – 800$ kg/m^2 s • $T_{sat} = 40$ °C • $x_{in} = 1$ • Constant $T_w = 30$ °C	• Steady • 3-D, 2-D axisymmetric • VOF • CSF • Lee model: $r_i = 7.5 \times 10^5 – 1 \times 10^7$ s^{-1} • low-*Re* SST k–ω turbulence model
Da Riva & Del Col (2012) [26]	• R134a • Horizontal, 1g_e • Circular channel with $D = 1$ mm and $L = 75$ mm • $G = 100$ kg/m^2 s • $T_{sat} = 40$ °C • $x_{in} = 1$ • Constant $T_w = 30$ °C	• Steady • 3-D • VOF • CSF • Lee model: $r_i = 7.5 \times 10^5$ s^{-1} • low-*Re* k–ω turbulence model
Chen et al. (2014) [27]	• FC-72 • Horizontal, 1g_e • Square channel with $A_c = 1$ mm $\times$ 1 mm and $L = 300$ mm, cooled along 3 walls • $G = 100 – 150$ kg/m^2 s • $T_{sat} = 60$ °C • $x_{in} = 1$ • Constant $q''_w = 10 – 30$ kW/m^2	• Transient • 3-D • VOF • CSF • Thermal equilibrium model: $f_o = 100$ s^{-1} K^{-1} • Realizable k–ε turbulence model
Qiu *et al.* (2014) [28]	• Steam • Vertical upflow, 1g_e • Tube with $D = 12$ mm and $L = 1.8$ m • $G = 100 – 6400$ kg/m^{2}s • $T_{sat} = 536 – 537.09$ • $x = 0.0 – 0.4$ • Constant $T_w = 535.09$ K	• Transient • 3-D • VOF • CSF • Lee model: $r_i = 10{,}000$ s^{-1} • RSM turbulence model
Lee *et al.* (2015) [29]	• FC-72 • Vertical downflow, 1g_e • Tube with $D = 11.89$ mm and $L = 0.8$ m • $G = 184.4 – 459.0$ kg/m^2 s • $T_{sat} = 58.4 – 75.0$ °C • $x_{in} = 1$ (4 – 7 °C superheated) • Polynomial for q''_w derived from experimental data	• Transient • 2-D axisymmetric • VOF • CSF • Lee model: $r_i = 10{,}000$ s^{-1} • SST k– ω turbulence model
Kharangate *et al.* (2016) [30]	• FC-72 • Vertical upflow, 1g_e • Tube with $D = 11.89$ mm and $L = 0.8$ m • $G = 58.4 – 271.5$ kg/m^2 s • $T_{sat} = 58.0 – 63.4$ °C • $x_{in} = 1$ (9 – 16 °C superheated) • Polynomial for q''_w derived from experimental data	• Transient • 2-D axisymmetric • VOF • CSF • Lee model: $r_i = 10{,}000$ s^{-1} • SST k– ω turbulence model
Li et al. (2017) [31]	• R410a • Horizontal, 0g_e – 1g_e • Tube with $D = 3.78$ mm and $L = 400$ mm • $G = 307 – 720$ kg/m^2 s • $T_{sat} = 320$ K • $x_{in} = 1$ • Constant $T_w = 310$ K	• Steady • 3-D • VOF • CSF • Lee model: $r_i = 1.5 \times 10^6$ s^{-1} • SST k– ω turbulence model

(*continued on next page*)

Table 1 (*continued*)

Authors	Geometry and operating conditions	Key models and parameters
Li et al. (2018) [32]	• R134a • Horizontal, $1g_e$ • Square channel with $A_c = 1$ mm × 1 mm and $L = 50 – 600$ mm • $G = 50 – 500$ kg/m^2 s • $T_{sat} = 40$ °C • $x_{in} = 1$ • Constant q''_w	• Steady • 3-D • VOF • CSF • Lee model: $r_i = 1000$ s^{-1} • k–ϵ turbulence model
Wu & Li (2018) [33]	• R32 • Horizontal, $1g_e$ • Tube with $D = 0.1$ mm and $L = 5$ mm • $G = 100 – 200$ kg/m^2 s • $T_{sat} = 60$ °C • $x_{in} = 0.5$ • Constant $T_w = 20$ °C	• Transient • 2-D, axisymmetric • VOF • CSF • Lee Model ○ $r_i = 3.3 \times 10^9$ s^{-1} • Laminar flow
Toninelli *et al.* (2019) [34]	• R134a • Horizontal and vertical Downflow, $1g_e$ • Tube with inlet $D = 3.4$ mm and $L = 136 – 900$ mm • $G = 50 – 200$ kg/m^2 s • $T_{sat} = 40$ °C • $x_{in} = 0.6 – 1$ • Constant $T_w = 30$ °C	• Steady and transient • 3-D and 2-D axisymmetric • VOF • CSF • Lee model: $r_i = 1 \times 10^5 – 6 \times 10^6$ s^{-1} depending on case • SST k-ω and low-Re k–ω turbulence model
Gu et al. (2019) [35]	• R1234ze(E) • Varied orientation from vertical upflow to vertical downflow, $1g_e$ • Tube with $D = 0.1$ mm and $L = 5$ mm • $G = 300 – 800$ kg/m^2 s • $T_{sat} = 313$ K • $x_{in} = 1$ • Constant $T_w = 303$ K	• Steady • 3-D • VOF • CSF • Lee model: $r_i = 4.5 \times 10^5 – 1.1 \times 10^6$ s^{-1} depending on case • SST k-ω turbulence model
Lei et al. (2020) [36]	• FC-72 • Horizontal, $1g_e$ • Rectangular channel with $A_c = 1$ mm × 1 mm and $L = 300$ mm, cooled along 3 walls • $G = 68 – 367$ kg/m^2 s • $T_{sat} = 57.2 – 62.3$ °C • $x_{in} = 1$ • Polynomial for q''_w derived from experimental data	• Transient • 3-D • VOF • CSF • Lee model: $r_i = 33{,}000$ s^{-1} • SST k-ω turbulence model
Qiu et al. (2020) [37]	• FC-72 • Microgravity • Tube with $D = 7.12$ mm and $L = 791.72$ mm • $G = 128.99 – 177.79$ kg/m^2 s • $T_{sat} = 333.48 – 335.56$ K • $x_{in} = 0.71 – 0.89$ • Polynomial for q''_w derived from experimental data	• Transient • 2-D axisymmetric • VOF • CSF • Lee model: $r_i = 10{,}000$ s^{-1} • SST k-ω turbulence model
Tang et al. (2020) [38]	• R410A • Horizontal, $1g_e$ • Tube with $D = 4.54$ mm and $L = 43.9$ mm (with micro-fin tubes containing either straight or helical fins on tube interior) • $G = 500 – 700$ kg/m^2 s • $T_{sat} = 320$ K • $x_{in} = 1$ • Constant $T_w = 310$ K	• Steady • 3-D • VOF • CSF • Lee model: $r_i = 1.5 \times 10^6$ s^{-1} • SST k-ω turbulence model
Lee et al. (2020) [39]	• HFO-1234yf • Horizontal, $1g_e$ • Converging tube with inlet $D = 4$ mm and $L = 600$ mm	• Steady • 3-D • VOF • CSF

Table 1 (*continued*)

Authors	Geometry and operating conditions	Key models and parameters
	• $G = 200 – 800$ kg/m^2 s • $T_{sat} = 288$ K • $x_{in} = 1$ • Constant $q''_w = 9.9 – 24.3$ kW/m^2	• Lee model: $r_i = 8 \times 10^5 – 3 \times 10^6$ s^{-1} depending on case • SST k-ω turbulence model
Dai et al. (2022) [40]	• Propane • Horizontal, $1g_e$ • Tube with $D = 4$ mm and $L = 900$ mm • $G = 180 – 360$ kg/m^2 s • $T_{sat} = 313 – 328$ K • $x_{in} = 1$ • Constant $T_w = 293 – 323$ K	• Steady • 3-D • VOF • CSF • Lee model: $r_i = 3000 – 10{,}000$ s^{-1} depending on case • SST k-ω turbulence model
He et al. (2023) [41]	• Neon • Horizontal, $0g_e$, $0.17g_e$, $0.38g_e$, $1g_e$ • Tube with inlet $D = 1$ mm and 2 mm, and $L = 0.25$ m • $G = 20 – 187$ kg/m^2 s • $T_{sat} = 24.5 – 44.5$ K • $x_{in} = 1$ • Constant $q_w = 7.5$ kW/m^2	• Transient • 3-D • VOF • CSF • Lee model: $r_i = 30{,}000$ s^{-1} • SST k-ω turbulence model

within the liquid sublayer between the slug bubbles and the wall. The local temperature gradient varied depending on whether the region was occupied by vapor or liquid. As the flow transitioned to churn flow, phase separation became less distinct, producing disordered temperature and velocity fields. In contrast, during wispy-annular and annular flow, both temperature and velocity profiles became more uniform and aligned with the flow direction. A steep temperature gradient across the thin condensate film was observed in these regimes, indicating highly efficient heat transfer.

Lee et al. [29] and Kharangate et al. [30] performed computational studies of FC-72 condensation within a tube of D = 11.89 mm under vertical downflow and vertical upflow conditions, respectively. To enhance numerical stability during liquid film initialization and expedite convergence, a thin condensate film was manually introduced at the location where the flow reached saturation ($x_e = 1$). The simulated temperature distribution across this film showed good agreement with the corresponding eddy diffusivity profile, which effectively attenuates turbulent fluctuations near both the wall and the liquid–vapor interface.

Li et al. [31] numerically investigated condensation of R410A in an isothermal horizontal tube with an inner diameter of D = 3.78 mm under varying gravity levels. Consistent with observations by other researchers, reducing the level of gravity led to a more circumferentially uniform condensate film and lower heat transfer coefficients at low mass fluxes. Under Earth gravity, the authors observed a buoyancy-induced vortex near the bottom of the vapor core, accompanied by liquid flow along the tube wall from the top toward the bottom of the channel. In microgravity, the streamlines were oriented radially outward, and small vortices formed within the liquid film at low vapor qualities. This flow behavior was attributed to vapor migration toward the liquid–vapor interface, which acts as a mass sink for the vapor phase.

Li et al. [32] numerically studied the effects of gravity and surface tension on the condensation of R134a in a horizontal square channel with a hydraulic diameter of $D_h = 1$ mm subjected to a constant wall heat flux. The influence of gravity was found to be negligible in short channels, where condensate redistribution was minimal. In longer channels, however, buoyancy caused liquid to accumulate along the bottom wall, producing a thicker film compared to the upper surface. Incorporating surface tension effects led to thinning of the condensate

film and consequently enhanced the overall heat transfer coefficient.

Wu and Li [33] investigated condensation of R32 within a microtube of D = 0.1 mm. In the annular flow regime, interfacial waves were generated by pressure fluctuations associated with bubble release from the vapor core. The amplitude of these ripples increased at higher flow rates, where viscous forces dominated over surface tension. However, the local heat transfer coefficient was found to be largely independent of flow rate and instead governed primarily by local vapor quality.

Toninelli et al. [34] conducted a series of numerical simulations examining condensation of R134a within an isothermal circular tube. Their simulations successfully reproduced interfacial waves and droplet entrainment phenomena observed in corresponding experiments, although these features were captured only under transient conditions. The presence of interfacial waves led to a reduction in the average liquid film thickness and an associated enhancement of the heat transfer coefficient. In contrast, steady-state simulations of horizontal flow produced a smooth liquid–vapor interface and stratified flow pattern, which reduced heat transfer in the lower portion of the channel.

Gu et al. [35] performed a computational study of R1234ze(E) condensation within an isothermal circular tube of D = 4.57 mm, examining various flow orientations ranging from vertical upflow to vertical downflow. Overall, the downflow orientation produced higher heat transfer coefficients and larger frictional pressure gradients compared to upflow. However, the influence of orientation on the heat transfer coefficient diminished at higher mass fluxes and vapor qualities, where inertial and shear effects became dominant.

Lei et al. [36] numerically investigated condensation of FC-72 in a horizontal square microchannel measuring 1 mm × 1 mm, with an axially varying cooling heat flux (derived from experimental data) applied to three of the channel walls. Their simulations successfully reproduced the observed flow patterns and predicted wall temperatures with an average deviation of less than 7 % relative to experimental measurements. At the lowest flow rate, rapid transitions between flow patterns produced large axial temperature gradients along the bottom wall, whereas higher flow rates yielded more uniform, nearly isothermal wall temperatures. Analysis of the simulated local fluid temperatures revealed a strong correlation between temperature distribution and the prevailing flow pattern.

Qiu et al. [37] simulated condensation of FC-72 within a circular tube of D = 7.12 mm subjected to a circumferentially uniform yet axially varying cooling heat flux. The flow entered the tube in an annular two-phase state. The authors demonstrated the effectiveness of the Lee model in accurately capturing phase-change dynamics. Although some deviations were observed in the local wall temperature predictions, the average wall temperatures exhibited good agreement with experimental measurements. The study concluded that fully three-dimensional CFD models are necessary to achieve high-fidelity predictions of condensation behavior; however, their substantial computational cost remains a significant limitation for large-domain simulations.

Tang et al. [38] conducted numerical simulations of R410A condensation within an isothermal micro-finned tube of D = 4.54 mm. Two fin geometries were examined: straight fins and helical fins with varying helix angles. As vapor quality decreased, the heat transfer coefficient correspondingly declined. However, the helical fin configurations generated a centrifugal force that promoted circumferential liquid redistribution, thereby enhancing heat transfer performance at low vapor qualities (below $x_e = 0.6$).

Lee et al. [39] computationally investigated the condensation of HFO-1234yf inside straight and converging isothermal tubes. During annular flow, interfacial ripples formed wavy liquid films, and portions of the film were shed as liquid ligaments that became entrained in the vapor core. In the converging tube, the condensate film was up to 15 % thinner due to stronger velocity gradients at the liquid–vapor interface. This thinning enhanced the heat transfer coefficient but also led to a 10 % increase in pressure drop.

Dai et al. [40] conducted computational simulations of propane condensation within an isothermal circular tube of D = 4 mm. The predicted heat transfer coefficients agreed with experimental measurements within 20 %. The authors reported that increasing mass velocity, decreasing saturation temperature, and increasing wall subcooling each enhanced the heat transfer coefficient, with wall subcooling exerting the strongest influence on both flow pattern and velocity distribution. At low wall subcooling, the flow remained annular; however, when wall subcooling was increased to 20 K, the flow transitioned to a plug flow pattern.

He et al. [41] numerically studied flow condensation of cryogenic neon inside horizontal tubes of D = 1 mm and 2 mm. They investigated gravity effect on condensation flow pattern, local condensate film distribution, and local and global heat transfer by comparing simulation results from zero gravity, Lunar gravity, Martian gravity, and Earth gravity. The study concluded that the liquid film becomes unstable in lower gravity level. Furthermore, under low mass velocity, the heat transfer is enhanced in the high vapor quality region, but it is deteriorated in low vapor quality region (below $x_e = 0.19$). The gravity effect is more significant in smaller tube diameters and decreases as mass velocity gets higher.

1.4. Objectives of present study

This study represents a collaborative effort between the Purdue University Boiling and Two-Phase Flow Laboratory (PU-BTPFL) and NASA Glenn Research Center, initiated in 2011 with the primary goal of developing the Flow Boiling and Condensation Experiment (FBCE). FBCE is NASA's largest and most complex phase-change facility ever designed for long-duration microgravity research and was successfully deployed aboard the International Space Station (ISS) in 2021. The mission of FBCE is to advance understanding of the effects of microgravity on flow boiling and flow condensation processes. As part of the FBCE campaign, Mudawar et al. [16] obtained long-duration, steady-state condensation data under microgravity conditions aboard the ISS, yielding a comprehensive heat transfer database exceeding 2000 data points and encompassing the full condensation spectrum—from superheated vapor upstream to subcooled liquid downstream. The present paper extends this effort through a detailed computational investigation of flow condensation in microgravity, focusing on the validation and application of numerical simulations of n-perfluorohexane (nPFH) condensation within the FBCE Condensation Module for Heat Transfer (CM-HT).

Simulations were first conducted for vertical downflow condensation using the Volume of Fluid (VOF) method to capture the development of a distinct liquid film along the condensing surface. Agreement between the predicted and experimentally measured wall temperatures was significantly improved by incorporating an interfacial shear model (implemented as a User-Defined Function (UDF)) to account for momentum transfer between the vapor core and the liquid film, thereby addressing certain limitations inherent in the standard VOF framework. The enhanced model was subsequently applied to simulate condensation within CM-HT under microgravity conditions. The model simulated flow condensation from low mass velocity of $G = 53.8$ kg/m^2 s up to high mass velocity of $G = 242.9$ kg/m^2 s. The results were validated against wall temperature measurements obtained during the CM-HT condensation experiments conducted under and aboard the ISS as part of the Flow Boiling and Condensation Experiment (FBCE). In addition to temperature validation, detailed analyses of local heat flux, interfacial morphology, and turbulence structure, which are difficult to measure in experiments, were conducted. The findings of this study support the present CFD model can give thorough understanding of flow condensation and be an accurate predictive tool for two-phase thermal systems in both microgravity and Earth gravity.

2. Experimental methods

The present study utilizes previously published experimental data obtained from the Condensation Module for Heat Transfer (CM-HT) to validate the results of the numerical simulations. This section provides a brief overview of the essential aspects of the experimental data collection methodology. Comprehensive descriptions of the flow loop design, test module configuration, experimental procedures, data reduction techniques, and measurement uncertainty analyses can be found in a previous detailed experimental paper [16].

2.1. Condensation module for heat transfer

Fig. 1 illustrates the Condensation Module for Heat Transfer (CM-HT), which functions as a counter-flow, tube-in-tube heat exchanger. The working fluid, n-perfluorohexane (nPFH), flows through the inner stainless-steel tube with an inner diameter of 7.24 mm, as shown in Fig. 1(a). Over an active condensation length of $L = 574.5$ mm, the nPFH rejects heat to a counter-flowing stream of cooling water. The water travels through the annulus formed between the tube's 7.94 mm outer diameter and a 12.70 mm diameter circular channel machined into a polycarbonate block that encases the tube. To reduce flow non-uniformities originating from the upstream 90° bend, a honeycomb straightener is installed immediately before the condensing section to align streamlines and suppress large-scale eddies. G10 plastic insulation sleeves are positioned upstream and downstream of the condensing length to minimize parasitic heat transfer between the nPFH and water streams. The polycarbonate housing consists of two clamped halves compressed between aluminum support plates, with thermocouples and pressure transducers integrated throughout CM-HT to facilitate detailed heat-transfer measurements.

The inlet and outlet temperatures of both the nPFH and cooling water are measured using type-E thermocouples inserted directly into the respective flow streams. Absolute pressure transducers monitor the nPFH pressure immediately upstream and downstream of the condensing section, while the cooling-water pressure is measured on both sides of the CM-HT. Along the length of the channel, the outer-wall temperature of the stainless-steel tube and the water temperature within

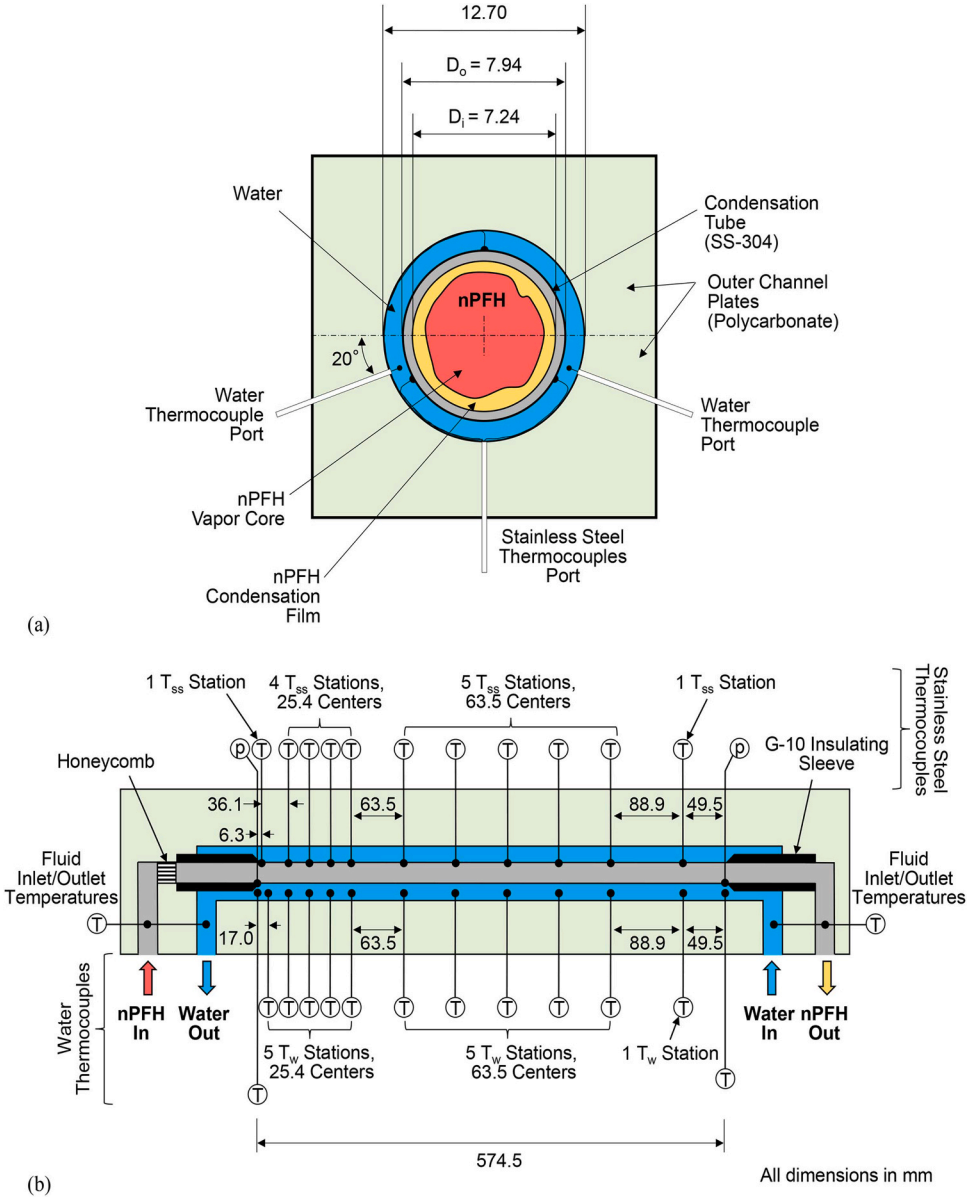

Fig. 1. Schematic representations of Condensation Module for Heat Transfer (CM-HT) depicting the (a) circumferential and (b) axial locations of thermocouples [16].

the annulus are recorded at eleven axial stations, as illustrated in Fig. 1 (b). The circumferential placement of thermocouples at each station is also shown in Fig. 1(b). Axial spacing between stations is reduced near the nPFH inlet to capture the rapid temperature variations associated with liquid-film formation and early condensation development.

2.2. Two-Phase flow loop and integration onboard the ISS

A schematic of the closed-loop system is presented in Fig. 2. The setup mirrors the flow-boiling loop of the FBCE [42], differing only in the test section. Circulation of the working fluid is maintained by a positive-displacement internal-gear pump. Immediately downstream, a Coriolis flowmeter measures the mass flow rate and provides feedback control to the pump's flow controller. The fluid then passes through a filter before entering the preheater, designated as the Bulk Heater Module (BHM), which raises the subcooled liquid to the desired inlet condition for the CM-HT. Within CM-HT, detailed heat-transfer measurements are obtained as the working fluid rejects heat to the counterflowing cooling water supplied by the ISS Thermal Control System (ITCS). The nPFH exits CM-HT either as a saturated two-phase mixture or as a subcooled liquid, depending on the test condition. Any residual heat added in the BHM is subsequently removed in a downstream liquid-to-water heat exchanger, referred to in Fig. 2 as the condenser. A static mixer positioned after the condenser ensures thermodynamic uniformity of the nPFH before it returns to the pump inlet. An accumulator, connected via a T-junction between the mixer and pump, establishes the system reference pressure and suppresses two-phase flow instabilities. Pressures and temperatures are continuously monitored at multiple locations throughout the loop using a combination of pressure transducers, thermocouples, and RTDs.

2.3. Operating procedure

All operations were conducted remotely from the NASA Glenn Research Center (GRC) Telescience Support Center using in-house control software. Once installed on the ISS, the payload required no crew intervention. During steady-state data acquisition, sensors sampled at 5 Hz, while a reduced sampling rate of 1 Hz was used during other periods. Data were routinely downlinked to GRC for analysis. Prior to each test day, the nPFH working fluid was degassed for several hours to remove noncondensable gases—a precautionary step to mitigate air ingress when the system rested in a sub-atmospheric state, as required by ISS safety protocols.

For each run, target inlet conditions were defined through the control software, specifying the nPFH mass velocity (G), inlet pressure (P_{in}), inlet temperature (T_{in}), thermodynamic equilibrium quality ($x_{e,in}$), and water mass velocity (G_w) referenced to the annular cross-section. The pump speed, accumulator air-side pressure, Bulk Heater Module (BHM) power, and ISS Thermal Control System (ITCS) valve settings were adjusted to achieve these setpoints. Once steady-state conditions were reached, data were recorded for five minutes at 5 Hz, and the final two minutes of each dataset were time-averaged to obtain the steady-state values reported herein. New operating points were then uploaded, and the procedure was repeated for subsequent runs.

3. Computational methods

3.1. Computational model and constitutive equations

This study employs ANSYS Fluent to perform two-dimensional, axisymmetric, transient simulations of condensation within the CM-

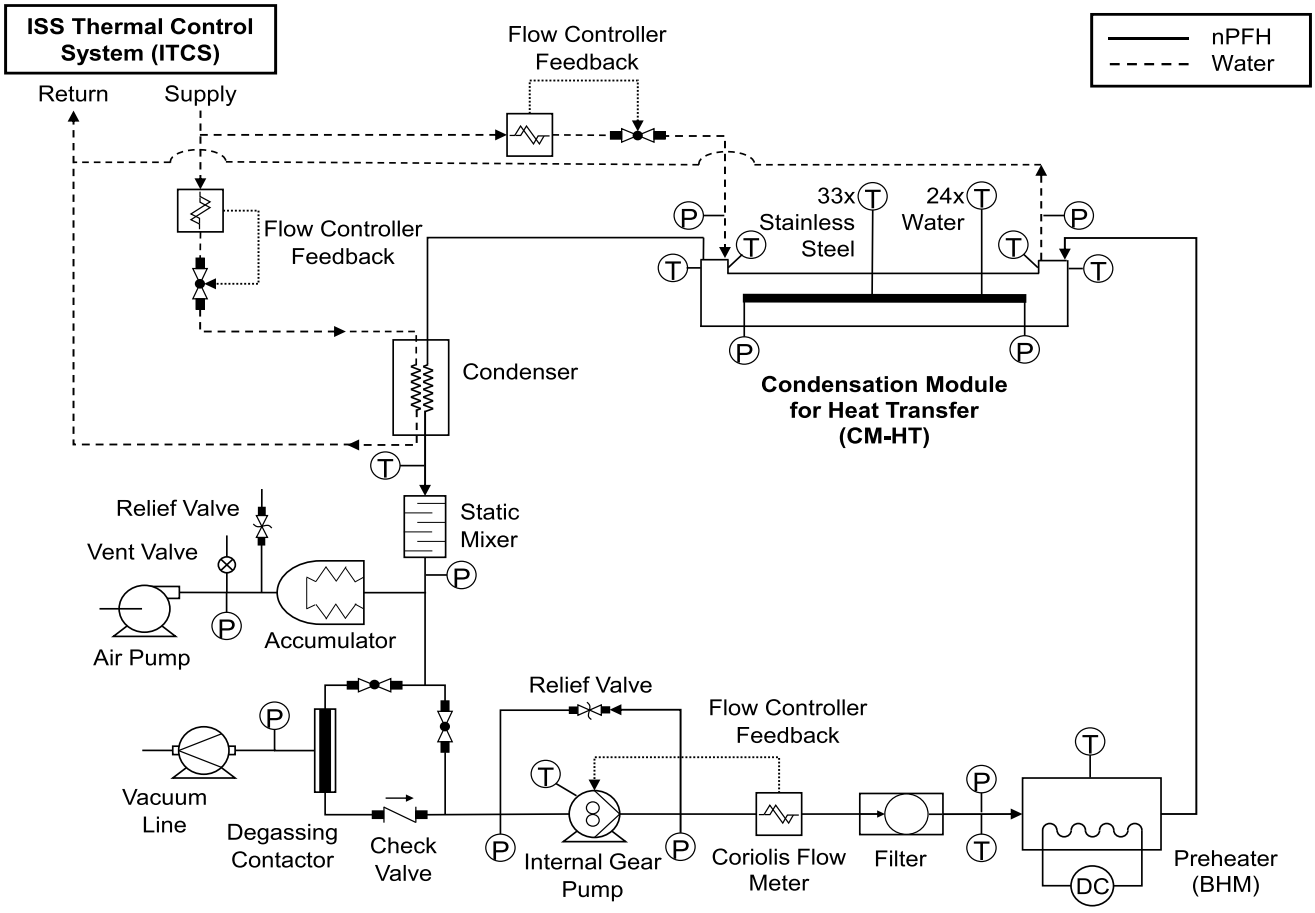

Fig. 2. Schematic diagram of two-phase flow loop used for flow condensation experiments [16].

HT. The transient analysis tracks the dynamic evolution of two-phase flow and heat transfer both across and along the heated length of the flow channel. To capture detailed interfacial behavior, interface tracking is implemented using the *Lee mass transfer model* in conjunction with the *Continuous Surface Force (CSF)* model within the transient Volume of Fluid (VOF) framework. The *Geo-Reconstruction scheme* (also referred to as the piecewise-linear method) is applied to maintain a sharply defined liquid–vapor interface and minimize artificial interfacial diffusion caused by numerical smearing.

Conservation of mass is solved separately for each phase, accounting for the transient variation and advection of the volume fraction, as well as the net interfacial mass transfer resulting from phase change within each computational cell. The governing equations for the liquid and vapor phases are expressed in Eq. (1) and Eq. (2), respectively.

$$\frac{\partial \alpha_f}{\partial t} + \nabla\cdot\left(\alpha_f \vec{u}_f\right) = \frac{1}{\rho_f}\sum\left(\dot{m}_{gf} - \dot{m}_{fg}\right), \tag{1}$$

and

$$\frac{\partial \alpha_g}{\partial t} + \nabla\cdot\left(\alpha_g \vec{u}_g\right) = \frac{1}{\rho_g}\sum\left(\dot{m}_{fg} - \dot{m}_{gf}\right), \tag{2}$$

where α, t, u, ρ, and $\dot{m}$, are volume fraction, time, velocity, density, and mass transfer rate by evaporation (with subscript of *fg*) and condensation (with subscript of *gf*), respectively. Notice that the sum of void fractions for the individual phases in each cell is equal to unity, meaning the Eq. (2) is not solved and the liquid volume fraction is computed as $\alpha_f = 1 - \alpha_g$. The physical properties appearing in the governing equations are expressed as functions of properties of individual phases weighted with respect to the volume fraction.

VOF solves a single momentum equation expressed as

$$\frac{\partial}{\partial t}(\rho u) + \nabla\cdot(\rho u u) = -\nabla P + \nabla\cdot\left[\mu\left(\nabla u + \nabla u^T\right)\right] - \sigma\kappa\delta(\varphi)\nabla\varphi + \rho g + \overline{F}, \tag{3}$$

where P, μ, $\bar{g}$, and $\overline{F}$ are the pressure, viscosity, gravitational acceleration, and additional body forces, respectively. Similarly, a single energy conservation equation, given in Eq. (4), is solved,

$$\frac{\partial}{\partial t}(\rho E) + \nabla\cdot(\vec{u}(\rho E + P)) = \nabla\cdot\left(k_{eff}\nabla T\right) + S_E, \tag{4}$$

where S_E is the latent heat transfer via phase change,

$$S_E = \dot{m}_{fg} h_{fg} \tag{5}$$

Interfacial mass transfer rates are computed using the Lee model [42],

$$\dot{m}_{fg} = r_i \alpha_f \rho_f \frac{(T_f - T_{sat})}{T_{sat}} \quad for\ evaporation \tag{6}$$

$$\dot{m}_{gf} = r_i \alpha_g \rho_g \frac{(T_{sat} - T_g)}{T_{sat}} \quad for\ condensation, \tag{7}$$

where r_i, T, and T_{sat} are the mass transfer intensity factor, temperature, and saturation temperature, respectively.

Because the predictive fidelity of the Lee phase-change model [43] is highly sensitive to the interfacial mass transfer coefficient (r_i), a parameter study was performed to identify a value that ensures both numerical stability and accurate prediction of condensation behavior for the present simulations. In a previous flow-condensation CFD investigation, Lei et al. [36] examined r_i values ranging from 300 to 33,000 s^{-1} and found that r_i = 33,000 s^{-1} provided the best agreement with measured wall and interfacial temperatures. Building on that result, the current analysis extended the range to higher values, testing four coefficients: 33,000, 50,000, 100,000, and 200,000 s^{-1}, as shown in Fig. 3.

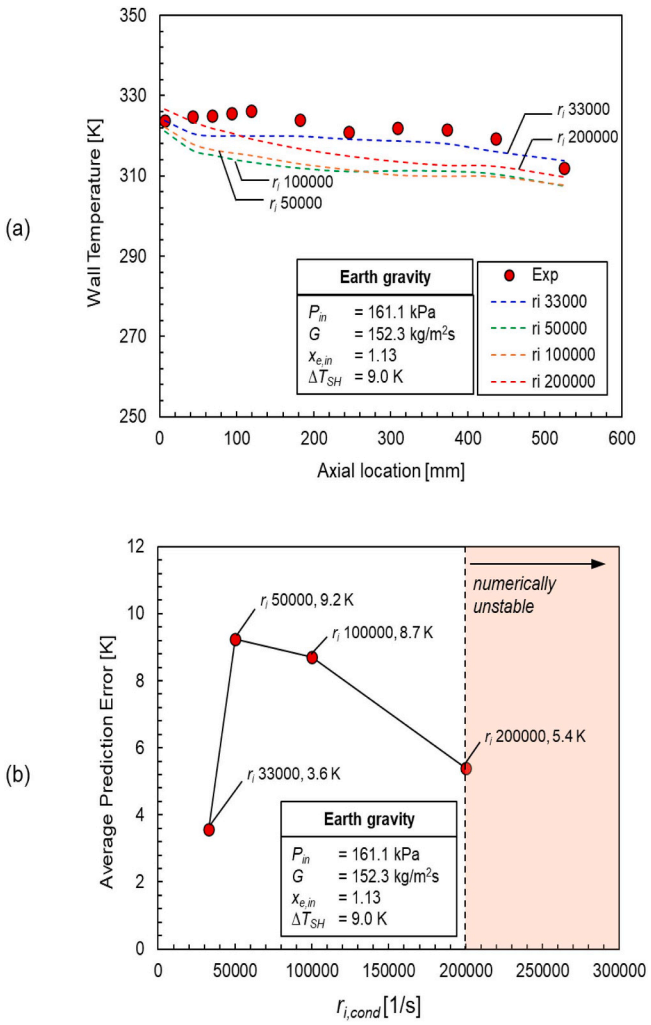

Fig. 3. $r_{i\,cond}$ value optimization test result showing (a) wall temperature comparison between measured streamwise temperature profile to predicted streamwise temperature profile with four different $r_{i\,cond}$ values, and (b) average prediction error with respect to $r_{i\,cond}$ value.

As illustrated in Fig. 3(a), the streamwise wall temperature profile predicted using r_i = 33,000 s^{-1} most closely matches the experimental data over the entire condensing length. To quantify this observation, Fig. 3(b) presents the mean absolute wall temperature error as a function of r_i. The minimum error occurs at r_i = 33,000 s^{-1}, whereas larger r_i values significantly overpredict the local phase-change rate, resulting in greater deviation from experimental results. Although r_i = 200,000 s^{-1} produced a comparable but slightly higher error, this setting led to numerical instability and eventual divergence. Therefore, balancing accuracy and robustness, r_i = 33,000 s^{-1} was selected for all simulations, with the same coefficient applied consistently to both condensation and evaporation source terms throughout this study.

Turbulence and eddy dissipation effects, including viscous heating, are modeled using the *Shear-Stress Transport (SST) k–ω turbulence model,* which offers superior near-wall resolution for multiphase flow simulations. The turbulent kinetic energy and specific dissipation rate in the SST k-w model can be expressed as

$$\frac{\partial}{\partial t}(\rho\kappa) + \nabla\cdot\left(\rho\vec{V}\kappa\right) = \nabla\cdot(\Gamma_\kappa\nabla\kappa) + \widetilde{G}_\kappa - Y_\kappa \tag{8}$$

$$\frac{\partial}{\partial t}(\rho\omega) + \nabla\cdot\left(\rho\vec{V}\omega\right) = \nabla\cdot(\Gamma_\omega\nabla\omega) + G_\omega - Y_\omega + D_\omega \tag{9}$$

where κ, ω, $\widetilde{G}_{\kappa}$, G_{ω} are the turbulent kinetic energy, specific dissipation rate, turbulent viscosity, generation of turbulence kinetic energy and generation of specific dissipation rate, respectively. Γ_{κ}, Γ_{ω}, Y_{κ}, Y_{ω}, D_{ω} are represent effective diffusivity of κ and ω, dissipation of κ and ω due to turbulence, and the cross-diffusion term, respectively.

3.2. Additional momentum source term: interfacial shear

An additional momentum source term, included in $\overline{F}$, is incorporated through a User-Defined Function (UDF) to enhance shear at the interface between the liquid film and vapor core. This term represents the interfacial shear stress and is formulated following the treatment proposed by Wallis [44], expressed as

$$\tau_i = \frac{1}{2} f_i \rho_g \left(\overline{u}_g - u_i\right)^2 + \frac{\left(\overline{u}_g - u_i\right)\Gamma_{gf}}{2p_{f,b}} \tag{10}$$

where τ_i, f_i, $\overline{u}_g$, u_i, Γ_{gf}, and $p_{f,b}$ denote the interfacial shear stress, interfacial friction factor, bulk vapor velocity, interfacial velocity, condensation rate per unit length, and interfacial perimeter, respectively. The interfacial friction factor f_i is determined using the correlation proposed by Shah et al. [45] and is calculated as

$$f_i = 16/\mathrm{Re}_c \; for \tag{11}$$

$$f_i = 0.079\mathrm{Re}_c^{-0.25} \; for \; 2000 \le \mathrm{Re}_c < 20000 \tag{12}$$

$$f_i = 0.046\mathrm{Re}_c^{-0.2} \; for \; \mathrm{Re}_c \ge 20000 \tag{13}$$

$$\mathrm{Re}_c = \rho_g \left(\overline{u}_g - u_i\right)(D - 2\delta) \Big/ \mu_g \tag{14}$$

Eqs. (11)–(14) are based on smooth interface assumption, neglecting the roughness effect from the fluctuating interface. The interfacial shear is applied in each cell that is considered to be at the phase interface. Since the cells are on a micrometer scale, the phase interface will be smooth, and influence of the interface fluctuations is minuscule. Therefore, smooth interface assumption is reasonable in the present model.

In order to apply interfacial shear calculated from Eq. (10) to the momentum term F in Eq. (3), the stress term should be converted into momentum term. The conversion of stress term at each cell into momentum term is expressed as

$$\overline{F} = \frac{\tau_i A_i}{V_{cell}} = \frac{\tau_i p_{f,b} \pi \Delta c}{A_{cell} \Delta c} = \frac{\tau_i p_{f,b} \pi}{A_{cell}} \tag{15}$$

where A_i, A_{cell}, and V_{cell} represent the area of the phase interface at the cell, cross-section area of the cell, and volume of the cell.

The influence of this additional momentum source term on the flow and heat transfer characteristics will be discussed in detail in a later section.

3.3. Computational domain and grid independence test

Fig. 4 shows the computational domain, which replicates the CM-HT test section depicted in Fig. 1. The model employs a two-dimensional, axisymmetric representation of the concentric tube geometry. The

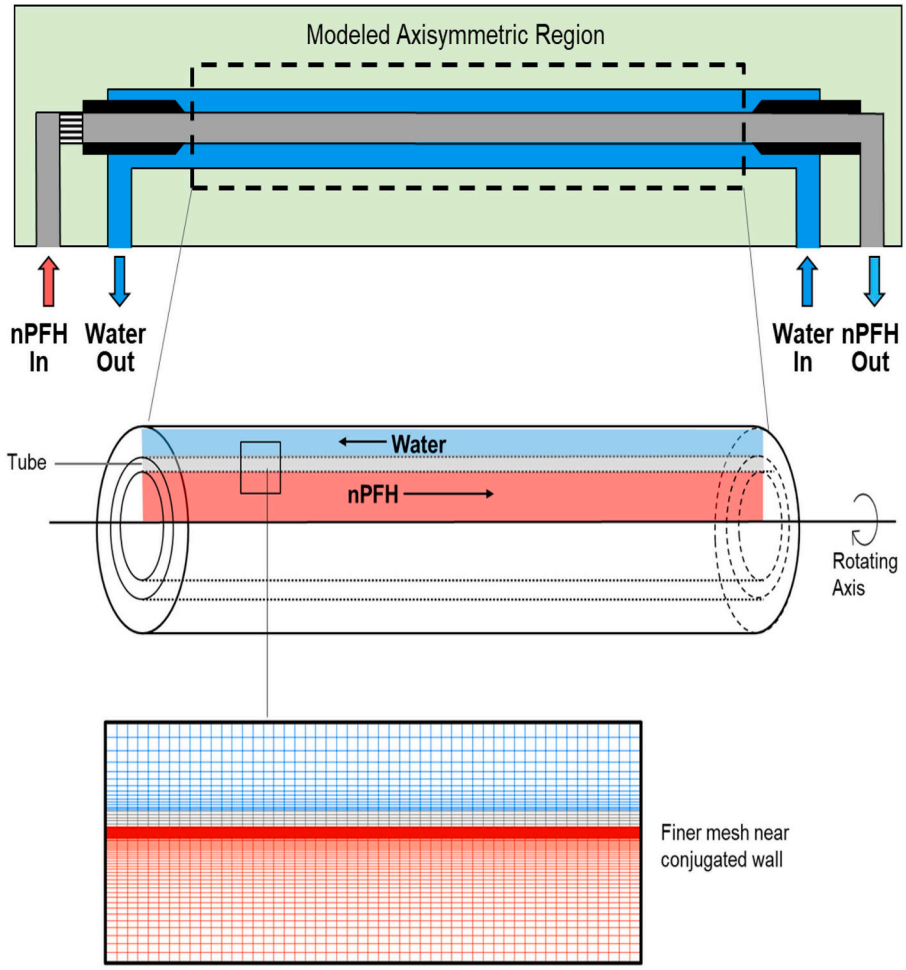

Fig. 4. Schematics for computational domain representing both nPFH and water flow channels with solid wall region for conjugated heat transfer.

working fluid, n-perfluorohexane (nPFH), flows through the inner tube with an inner diameter of 7.24 mm over a condensing length of 574.5 mm. The coolant water flows countercurrently through the annulus formed by the 7.94 mm outer diameter of the inner tube and a surrounding circular channel of 12.70 mm diameter. The axisymmetric formulation substantially reduces computational cost while accurately preserving the essential geometric characteristics of the experiment. The domain includes a 0.35 mm thick stainless-steel wall to enable conjugate heat transfer between the solid and fluid regions. A non-uniform mesh is applied, with near-wall refinement to resolve the viscous sublayer and accurately capture interfacial gradients critical to filmwise condensation.

Fig. 5 summarizes the results of the grid independence assessment. Fig. 5(a) compares the streamwise wall temperature profiles obtained using four different grid resolutions, ranging from 1 μm to 12 μm. The 1 μm grid provides the closest agreement with the experimentally measured wall temperatures along the entire condensing length. This trend is further illustrated in Fig. 5(b), which presents the mean absolute wall-temperature error between the CFD predictions and experimental data as a function of grid size. A clear reduction in error is observed as the grid is refined. Consequently, the 1 μm grid was selected for all subsequent simulations, as it yielded the lowest average wall-temperature error of 2.2 K.

It is worth noting that larger grid sizes, ranging from 20 μm to 100 μm, were previously examined by Lei et al. [36] for flow condensation simulations under similar conditions. Their study reported significantly higher prediction errors for grid sizes exceeding 20 μm. When these findings are considered in conjunction with the present grid independence results, it can be concluded that a 1 μm grid provides the optimal resolution within the investigated range of 1–100 μm, offering the best balance between accuracy and computational efficiency.

3.4. Boundary conditions

In this study, six simulation cases were performed, as summarized in Table 2. Pre-calculated fully developed velocity profiles and the corresponding turbulent properties were imposed at the inlet of the fluid domain as boundary conditions. All wall boundaries were assigned no-

Table 2
Summary of boundary conditions for six different cases.

Case #	Gravity	$\dot{m}$	G	P_{in}	$x_{e,in}$	T_{in}	$T_{sat,in}$
1	$1g_e$	2 g/s	53.8 kg/m^2 s	159.9 kPa	1.09	76.2 °C	71.3 °C
2	$1g_e$	4 g/s	102.1 kg/m^2 s	159.7 kPa	1.13	80.2 °C	71.3 °C
3	$1g_e$	6 g/s	152.3 kg/m^2 s	161.1 kPa	1.13	80.6 °C	71.6 °C
4	$0g_e$	3 g/s	72.8 kg/m^2 s	152.8 kPa	1.07	75.8 °C	69.8 °C
5	$0g_e$	6 g/s	145.7 kg/m^2 s	154.5 kPa	1.07	76.8 °C	70.2 °C
6	$0g_e$	10 g/s	242.9 kg/m^2 s	160.2 kPa	1.06	80.0 °C	71.4 °C

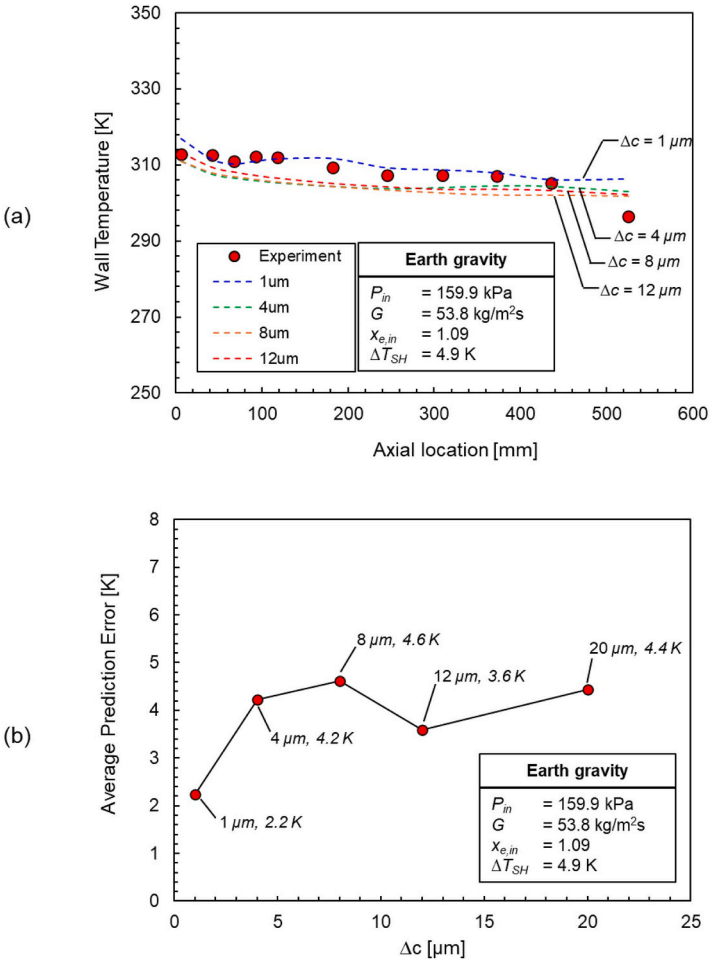

Fig. 5. Grid independence test results showing (a) wall temperature comparison between measured streamwise temperature profile to predicted streamwise temperature profile with four different grid sizes, and (b) average prediction error with respect to grid sizes.

slip conditions, while coupled heat-flux boundary conditions were applied at the solid–fluid interfaces to account for conjugate heat transfer. The inlet and outlet boundaries were specified by the imposed inlet velocity and outlet pressure, respectively. To ensure numerical stability and convergence, a global Courant number of 0.7 was maintained, and an adaptive time-stepping scheme was employed with minimum and maximum time steps of 10^{-7} s and 10^{-5} s, respectively.

Fig. 6 presents representative radial profiles of axial velocity and temperature obtained from the flow condensation simulations. As illustrated in Figs. 1 and 4, n-perfluorohexane (nPFH) enters the CM-HT as superheated vapor, flows through the stainless-steel tube while rejecting heat to a counterflowing water stream in the surrounding annulus, and exits as either a two-phase mixture or a subcooled liquid. The profiles shown correspond to z = 0.25 m for Case 4 in Table 2. The temperature decreases monotonically from the nPFH vapor core, across the stainless-steel wall, and into the water coolant—behavior consistent with filmwise condensation under conjugate heat transfer conditions. Because both the working fluid and coolant are explicitly modeled, the local condensation heat flux q'' can be directly evaluated, as indicated by the red arrow in Fig. 6, and later compared with experimentally fitted results. Furthermore, key interfacial transport quantities—including interfacial temperature and velocity, void fraction, and turbulence attenuation in the interfacial region—are quantified and analyzed in subsequent sections.

4. Results and discussion

4.1. Effect of added shear UDF on flow condensation simulation

Interfacial shear at the liquid–vapor boundary plays a critical role in governing liquid-film evolution and, consequently, heat transfer performance during flow condensation. The significant velocity slip between the vapor core and condensate film induces a tangential stress that drags the liquid along the surface, thinning the film, reducing its thermal resistance, and thereby enhancing the local heat transfer coefficient. However, conventional VOF formulations are known to inadequately represent interfacial momentum exchange and relative phase velocities, since a single momentum equation is solved for the mixture rather than for each individual phase [46]. To address this limitation, a User-Defined Function (UDF) was developed and implemented to augment the interfacial shear source term within the VOF framework, as described in Section 3.2. The fidelity of the enhanced model was evaluated by comparing its predictions against those obtained from the baseline VOF solver without the UDF.

Fig. 7 presents the streamwise wall temperature profiles for Case 1 in Table 2, comparing the CFD predictions with the experimentally measured wall temperatures. Near the inlet region, where condensation initiates and vapor–liquid slip is most pronounced, the baseline model underpredicts the wall temperature by approximately 4–10 K over z = 0–200 mm. Incorporation of the UDF significantly reduces this discrepancy, yielding much closer agreement with the experimental data. This improvement reflects the physical mechanism by which enhanced interfacial shear thins the condensate film, thereby reducing the wall-to-interface temperature difference. Farther downstream, as condensation progresses, the vapor-core velocity decreases and interfacial shear weakens, causing the UDF and baseline predictions to converge. Collectively, these results demonstrate that augmenting the VOF framework with the interfacial shear source term substantially improves the predictive accuracy of the flow condensation model. Consequently, the UDF-enhanced VOF formulation was employed for all subsequent simulations in this study.

4.2. Model validation

4.2.1. Earth gravity

The predictive accuracy of the present computational model was assessed by comparing the simulated wall temperature profiles with experimental measurements at each mass velocity under both Earth gravity and microgravity conditions. Fig. 8 presents the comparison for Earth gravity. In both the experimental data and numerical predictions, the wall temperature is highest near the inlet and gradually decreases downstream as the condensate film develops and the vapor velocity diminishes along the axial direction. The computational model reproduces this behavior with high fidelity, yielding a maximum average deviation of no more than 5.1 K from the experimental wall temperature measurements.

As shown in Fig. 8(a), the simulation for the lowest mass velocity case exhibited the highest overall prediction accuracy, with an average error of only 2.2 K and strong agreement across most of the condensing length. However, a maximum deviation of 9.8 K was observed near the

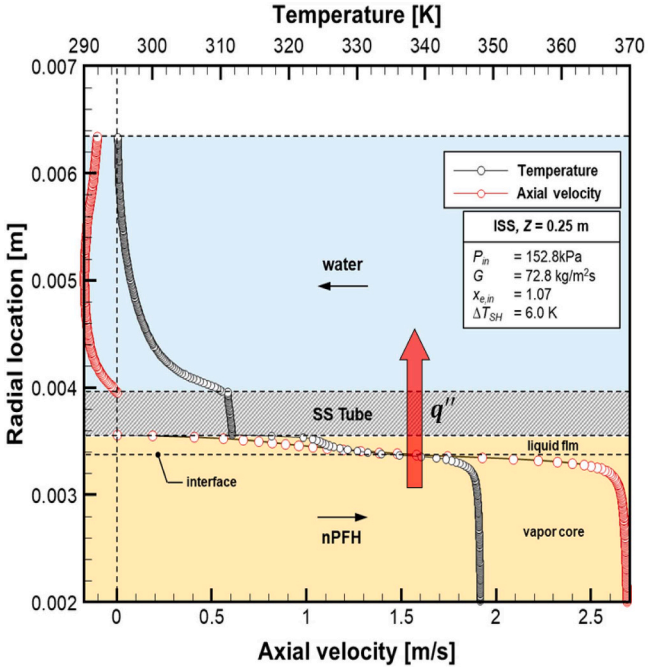

Fig. 6. Overview of predicted radial temperature and velocity profiles across the full radial range covering three domains: nPFH, stainless-steel tube, and water domains.

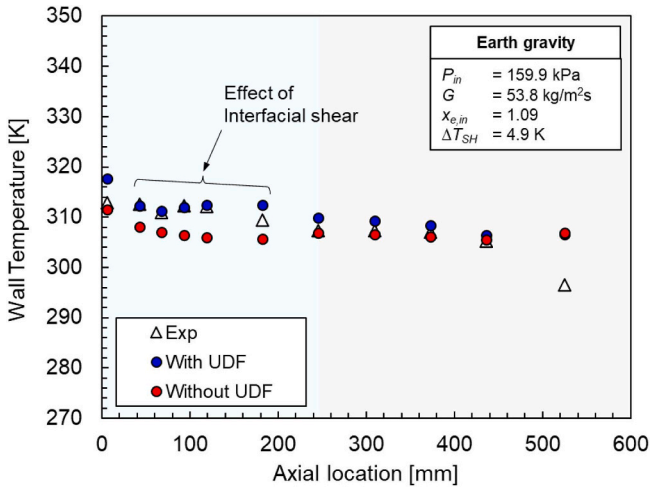

Fig. 7. Comparison of streamwise wall temperature predictions against experimentally measured wall temperature data both with and without the UDF.

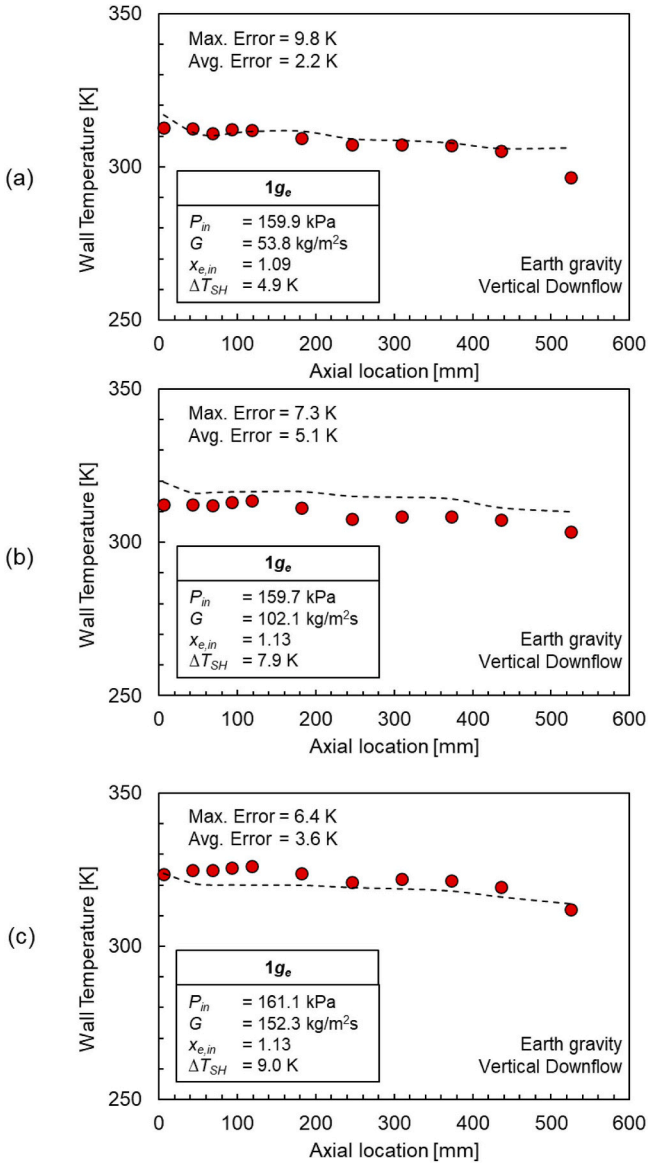

Fig. 8. Comparison of streamwise wall temperature predictions against experimentally measured wall temperature data for (a) $G = 53.8$ kg/m^2 s, (b) $G = 102.1$ kg/m^2 s, and (c) $G = 152.3$ kg/m^2 s under Earth gravity.

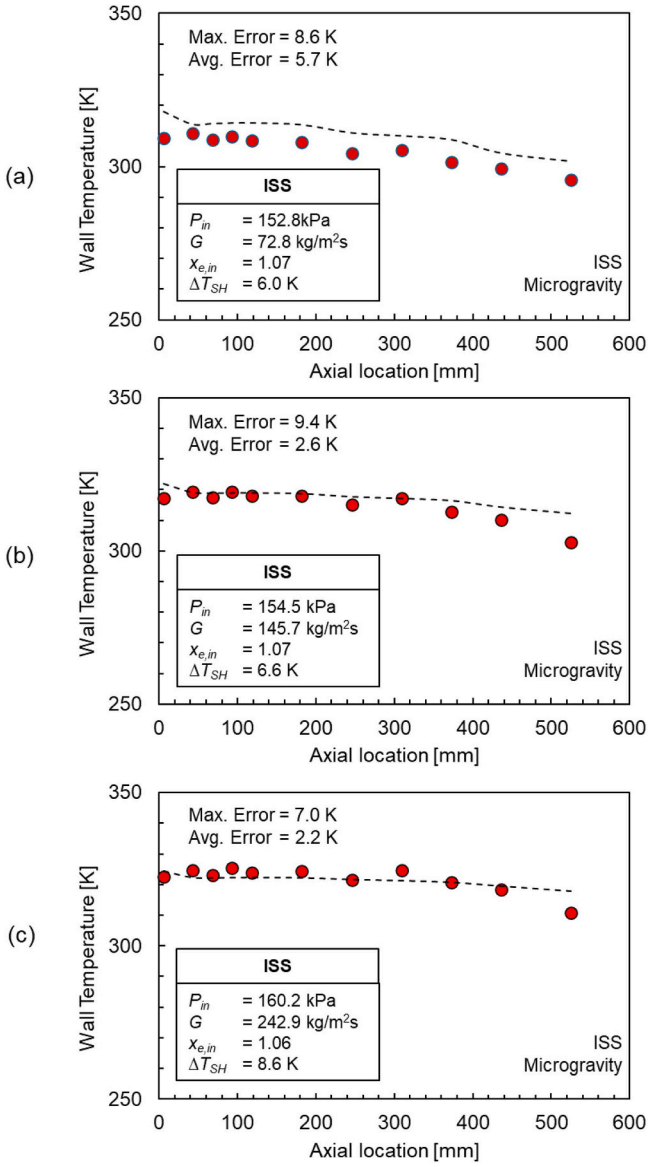

Fig. 9. Comparison of streamwise wall temperature predictions against experimentally measured wall temperature data for (a) $G = 72.8$ kg/m^2 s, (b) $G = 145.7$ kg/m^2 s, and (c) $G = 242.9$ kg/m^2 s under microgravity.

downstream end. This discrepancy corresponds to the region where the experimentally measured wall temperature dropped sharply, indicating that condensation had largely ceased and the flow transitioned to a single-phase liquid regime. Because the present computational model is formulated specifically for condensation heat transfer, its predictive accuracy diminishes once condensation is complete. In Fig. 8(b) and (c), representing higher mass velocity cases, the average error increased slightly; however, the overall wall temperature trends remained in good agreement with experimental results. Moreover, the downstream discrepancies were substantially reduced at higher mass velocities, as condensation persisted closer to the outlet under these conditions.

4.2.2. Microgravity

Fig. 9 presents the wall temperature validation results for the microgravity cases. Under microgravity, the condensate film tends to thicken due to the absence of buoyancy and the greater relative influence of surface tension. Consequently, even though the mass velocities were higher than those in the Earth gravity cases, the wall temperature exhibited a pronounced decrease in the downstream region, indicating reduced condensation activity. The maximum local error in the microgravity simulations occurred in this region, consistent with the downstream deviations observed for the lowest mass velocity case under Earth gravity. Nevertheless, the overall predictive accuracy in microgravity remained satisfactory, with a maximum average error of 5.7 K, comparable to the 5.1 K value obtained under Earth gravity. Furthermore, as shown in Fig. 9(b) and (c), corresponding to the higher mass velocity cases, the computational model demonstrated excellent agreement with experimental data, yielding average errors of 2.6 K and 2.2 K, respectively. These results confirm that the present computational model provides accurate predictions of condensation behavior under both Earth gravity and microgravity conditions.

4.3. Flow condensation predictions for other parameters

4.3.1. Predicted wall heat flux profiles

CFD is extensively used in multiphase flow research because it enables the prediction of parameters that are difficult or impossible to measure experimentally, such as local heat flux, interfacial morphology,

and turbulence structure. Fig. 10 compares the predicted wall heat flux distribution with the experimentally fitted data. In many prior computational studies of condensation heat transfer, a constant wall heat flux boundary condition was imposed along the condensing surface without explicitly modeling the coolant flow [47,48]. While this simplification improves numerical stability and reduces computational cost, it limits the physical realism of the simulation. In contrast, the present study explicitly models the counterflow of both the working fluid and coolant, as illustrated in Fig. 6, thereby more accurately reproducing the experimental boundary conditions and capturing the true conjugate heat transfer behavior during flow condensation.

As shown by the fitted experimental data [16], the wall heat flux varies along the condensation length. In the upstream region, where condensation is most active, the wall heat flux either increases or remains high as turbulence intensifies and the liquid film develops. Downstream, as condensation diminishes and the flow gradually transitions toward a single-phase regime, the wall heat flux correspondingly decreases. Especially, the measured wall heat flux significantly drops and approaches zero as it gets closer to the water inlet, showing big error and mismatching trend with the simulation. This discrepancy can be explained by uncertainty of the measurement method of wall heat flux in the experiment near the water inlet. The fitted wall heat flux data from the experiment was calculated using the water temperature gradient profile along the flow direction. Near the water inlet, the thermal boundary layer of water is still developing. Since the thermocouples measure the average water temperature, the measured water temperature gradient will be lower than the water temperature gradient near the wall. Therefore, the measured wall heat flux will be lower than the actual value and will get closer to zero as it gets closer to the water inlet. Furthermore, as noted in the previous section, the present computational model exhibits relatively higher prediction error in the downstream region. However, considering the region where condensation is active, and the thermal boundary layer of water is fully developed (0 ~ 400 mm), the present model accurately captures the wall heat flux distribution and reproduces the experimental trend.

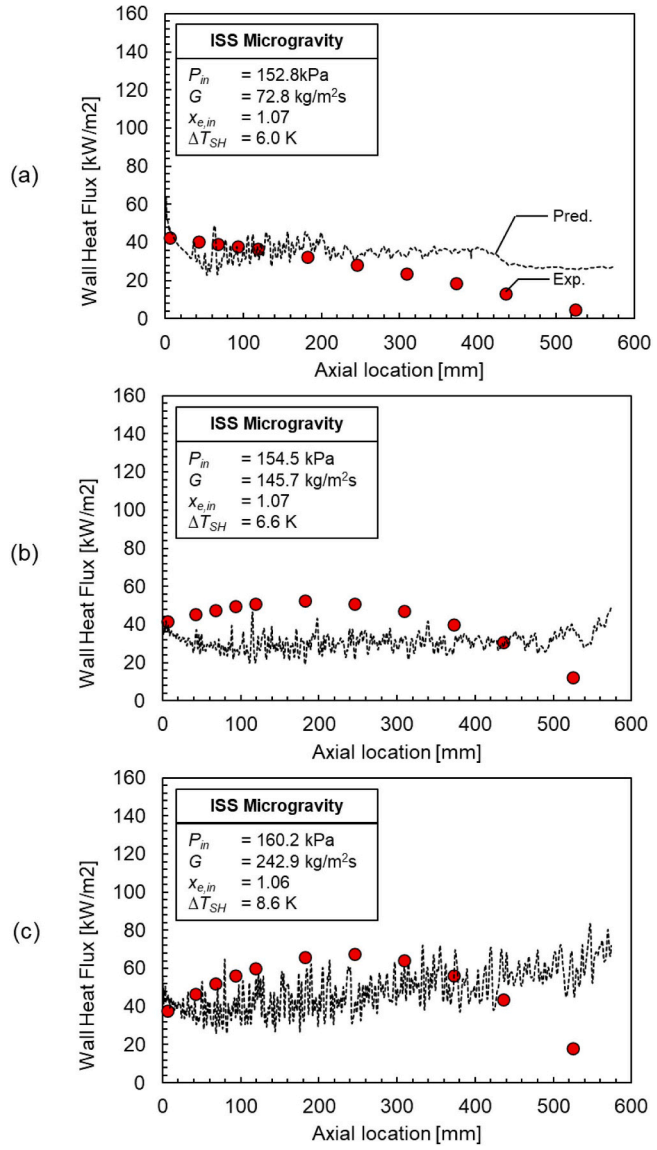

Fig. 10. Wall heat flux predicted from the computational model for (a) G = 72.8 kg/m^2 s, (b) G = 145.7 kg/m^2 s, and (c) G = 242.9 kg/m^2 s under microgravity.

In Fig. 10(a), the predicted wall heat flux shows good agreement with experimental results up to the point where the heat flux begins to decrease in the lowest mass velocity case. The downstream decline is also well captured. In Fig. 10(b) and (c), corresponding to higher mass velocities, the predicted wall heat flux is slightly lower than the experimental values in the upstream region; however, the average wall heat flux remains comparable. In all cases, the simulations reproduce the characteristic pattern of wall heat flux increasing and then decreasing along the condensation length. Overall, the model reflects the spatial variation of wall heat flux during condensation, offering a more realistic representation than simulations employing a fixed heat flux boundary condition, while maintaining acceptable error levels.

4.3.2. *Predicted interface profiles*

Computational analysis serves as a powerful tool for investigating interfacial physics, which is fundamental to understanding two-phase heat transfer mechanisms. Fig. 11 presents the distributions of void fraction, interface thickness, fluid temperature, and axial velocity near the phase interface under Earth gravity. As mass velocity increases, the velocity gradient across the interface becomes steeper. The larger velocity difference between the liquid and vapor phases enhances interfacial shear, which in turn exerts a stronger tangential drag on the condensate film. This increased shear thins the liquid film and suppresses droplet entrainment into the vapor core, resulting in a reduced interfacial thickness at higher mass velocities. Furthermore, because the liquid film acts as a thermal resistance layer, its thinning leads to a lower interface temperature and a steeper temperature gradient across the liquid–vapor boundary. Consequently, the condensation heat transfer coefficient increases with mass velocity due to the reduction in overall thermal resistance. The interfacial characteristics and flow behavior predicted by the present computational model show good agreement with observations from previous flow visualization studies reported in the literature [49,50].

Fig. 12 presents the interfacial profiles under microgravity conditions. Overall, the trends of velocity, temperature, and void fraction gradients across the interface are similar to those observed under Earth gravity, exhibiting steeper gradients with increasing mass velocity. However, a notable difference appears in the lowest mass velocity case. As shown in Figs. 11(a) and 12(a), despite the higher mass velocity in microgravity, the void fraction gradient is steeper than that in Earth gravity. Under microgravity, surface tension becomes the dominant interfacial force due to the absence of buoyancy, promoting droplet entrainment and leading to a thicker liquid–vapor interface characterized by larger droplets. At higher mass velocities, Fig. 12(b) and (c), this behavior is no longer observed, indicating that the influence of gravity diminishes as inertial forces increase. The slightly thicker interface seen in the highest mass velocity case compared to the mid-range case can be attributed to enhanced interfacial wave motion resulting from increased turbulence intensity. The gravity-dependent trends identified in this study show strong consistency with the flow visualization observations reported by Berto et al. [13].

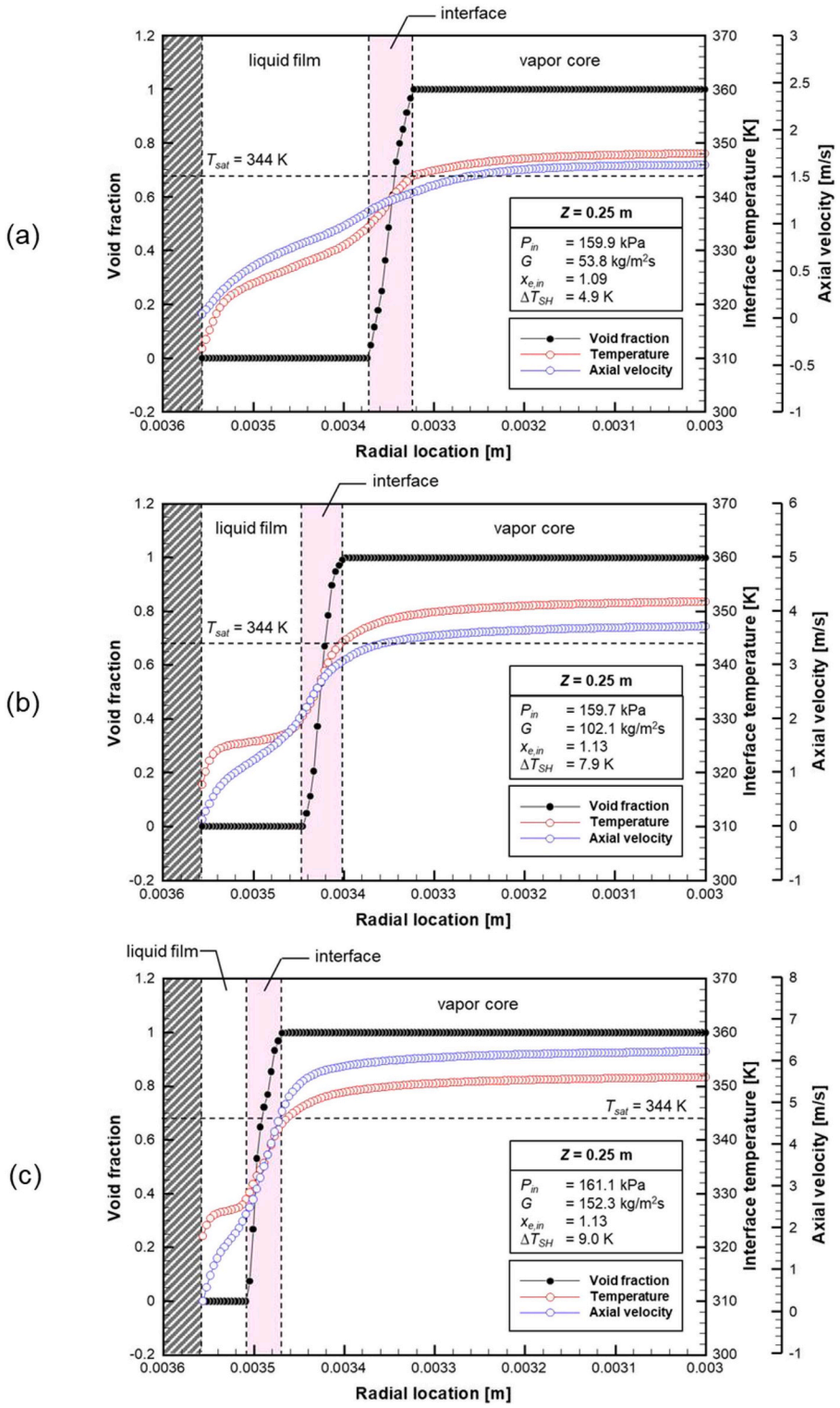

Fig. 11. Interfacial profiles predicted from the computational model for (a) $G = 53.8$ kg/m^2 s, (b) $G = 102.1$ kg/m^2 s, and (c) $G = 152.3$ kg/m^2 s under Earth gravity.

4.3.3. Predicted turbulence profiles

Understanding turbulence is crucial in condensation processes, as turbulent eddies significantly enhance the heat transfer coefficient. Computational modeling provides valuable access to turbulence parameter profiles that are difficult to obtain experimentally. Fig. 13 illustrates the turbulence characteristics near the liquid–vapor interface under microgravity conditions. The profiles obtained in the present study align well with those reported in previous research on interfacial turbulence damping [51].

As shown in Figs. 13(a) and (b), the turbulent kinetic energy and eddy viscosity profiles exhibit similar trends: both approach zero at the wall and at the phase interface while reaching peak values within the middle of the liquid film. Turbulence near the wall is suppressed due to dominant viscous forces, whereas at the phase interface, velocity fluctuations are strongly damped by surface tension, causing viscous effects to prevail—analogous to behavior near the solid boundary. The specific

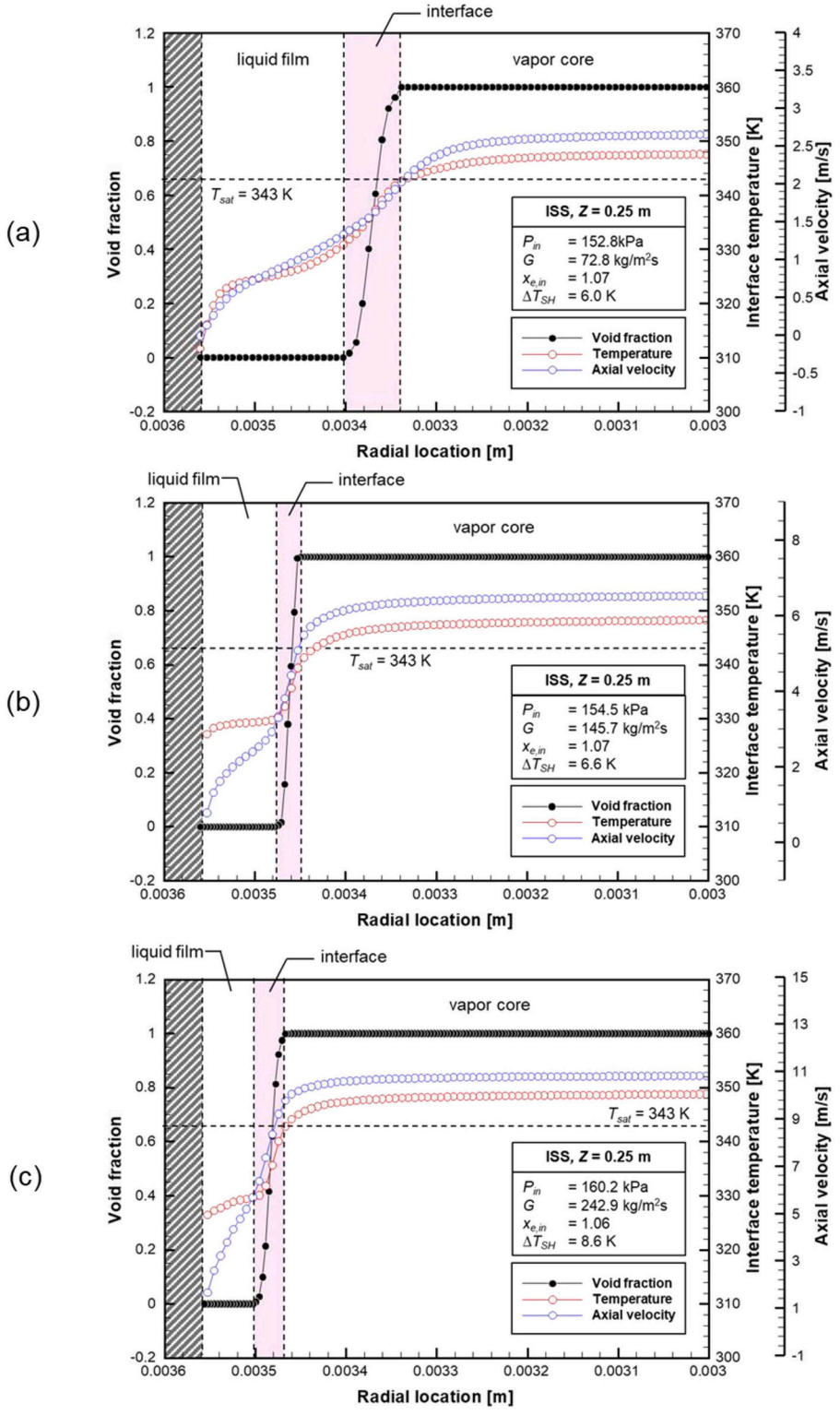

Fig. 12. Interfacial profiles predicted from the computational model for (a) $G = 72.8$ kg/m^2 s, (b) $G = 145.7$ kg/m^2 s, and (c) $G = 242.9$ kg/m^2 s under microgravity.

dissipation rate profile further indicates that turbulent energy is dissipated and converted into sensible heat at the interface, contributing to the steep temperature gradient observed in this region.

5. Conclusions

This study presents the validation and results of numerical simulations of n-perfluorohexane (nPFH) condensation within the Condensation Module for Heat Transfer (CM-HT). The computational framework improves upon the conventional Volume of Fluid (VOF) model by incorporating an interfacial shear term between the vapor core and liquid film, implemented through a User-Defined Function (UDF). The influence of this UDF was evaluated by comparing results from the enhanced model against those obtained using the baseline VOF formulation without the added shear treatment. The validated model was subsequently applied to simulate condensation within the CM-HT under

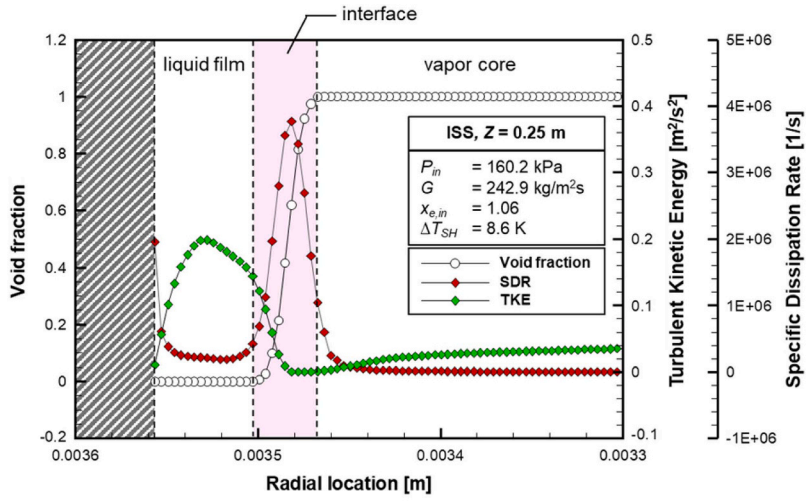

(a)

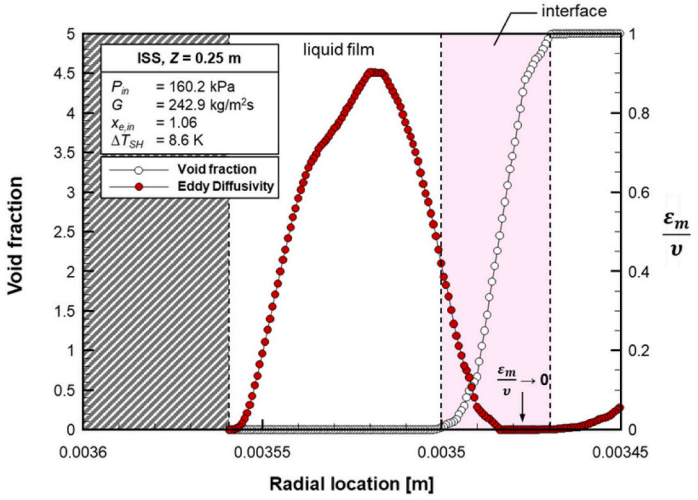

(b)

Fig. 13. Turbulence profiles predicted from the computational model for $G = 242.9$ kg/m^2 s under microgravity.

both microgravity conditions, during CM-HT condensation experiments conducted aboard the International Space Station as part of the Flow Boiling and Condensation Experiment (FBCE), and Earth gravity conditions. The model simulated low mass velocity of $G = 53.8$ kg/m^2 s up to high mass velocity of $G = 242.9$ kg/m^2 s. In addition to temperature validation, detailed analyses of wall heat flux distributions, interfacial transport behavior, and turbulence characteristics were presented. The developed computational model demonstrates strong capability in predicting heat transfer behavior during condensation and provides valuable physical insights into two-phase flow mechanisms in both Earth gravity and microgravity. The key findings of this study are summarized as follows:

(1) Incorporating interfacial shear through the User-Defined Function (UDF) improves the VOF model's tendency to underpredict wall temperatures in the upstream region. The enhanced interfacial shear increases the tangential drag exerted by the vapor core on the liquid film, resulting in a thinner condensate layer and a reduced temperature difference between the wall and the saturation interface. The influence of the UDF is most pronounced near the condensation onset, where vapor velocities are highest, and gradually diminishes downstream as the vapor core velocity decreases with condensation progression.

(2) The simulation results show good agreement with experimental data, with maximum average wall-temperature deviations of 5.1 K under Earth gravity and 5.7 K under microgravity. The largest local errors typically occur in the downstream region, where condensation diminishes and the flow transitions to a single-phase liquid regime.

(3) In the present computational model, both the working fluid and coolant were explicitly modeled in a counterflow configuration, rather than imposing a constant wall heat flux boundary condition. The predicted wall heat flux distribution aligns well with the experimentally fitted data in regions where condensation is active. Moreover, the model successfully captures the spatial variation of wall heat flux along the condensing wall, offering a more realistic representation of the heat transfer process compared to the fixed-flux approach.

(4) Analysis of the interfacial profiles reveals that stronger interfacial shear at higher mass velocities enhances liquid-film drag and suppresses droplet entrainment, thereby reducing both the liquid-film thickness and the overall interfacial thickness. At low mass velocities, however, droplet entrainment is promoted under

microgravity conditions due to the dominant influence of surface tension. As mass velocity increases, inertial forces become more significant, rendering the effects of gravity negligible.

(5) The turbulent kinetic energy and eddy diffusivity are both significantly damped near the wall and the liquid–vapor interface. Turbulence suppression at the interface results from dominant surface tension forces, causing viscous effects to prevail in a manner similar to that near the solid wall. The specific dissipation rate profiles further indicate that turbulent energy is dissipated and converted into sensible heat at the interface.

Data availability

The experimental raw data used in this paper will be publicly made available in a future NASA repository.

CRediT authorship contribution statement

Hyun Sung Hwang: Writing – review & editing, Writing – original draft, Visualization, Validation, Software, Methodology, Investigation, Formal analysis, Conceptualization. **Sunjae Kim:** Writing – review & editing, Writing – original draft, Visualization, Validation, Software, Methodology, Investigation, Formal analysis, Conceptualization. **Steven Darges:** Writing – review & editing, Writing – original draft, Validation, Software, Methodology, Investigation, Formal analysis, Data curation, Conceptualization. **Issam Mudawar:** Writing – review & editing, Writing – original draft, Validation, Supervision, Resources, Project administration, Methodology, Investigation, Funding acquisition, Data curation, Conceptualization.

Declaration of competing interest

The authors declare that they have no known competing financial interests or personal relationships that could have appeared to influence the work reported in this paper.

Acknowledgements

The authors acknowledge the support of the National Aeronautics and Space Administration (NASA) under grant no. 80NSSC22K0328.

References

[1] F.P. Chiaramonte, J.A. Joshi, Workshop on Critical Issues in Microgravity Fluids, Transport, and Reaction Processes in Advanced Human Support Technology – Final Report, NASA TM-2004-212940, Washington, D.C., USA, 2004.
[2] T.J. LaClair, I. Mudawar, Thermal transients in a capillary evaporator prior to the initiation of boiling, Int. J. Heat Mass Transf. 43 (2000) 3937–3952.
[3] G. Liang, I. Mudawar, Pool boiling critical heat flux (CHF) – Part 2: assessment of models and correlations, Int. J. Heat Mass Transf. 117 (2018) 1368–1383.
[4] I. Mudawar, R.A. Houpt, Mass and momentum transport in smooth falling liquid films laminarized at relatively high Reynolds numbers, Int. J. Heat Mass Transf. 36 (1993) 3437–3448.
[5] W.P. Klinzing, J.C. Rozzi, I. Mudawar, Film and transition boiling correlations for quenching of hot surfaces with water sprays, J. Heat Treat. 9 (1992) 91–103.
[6] M.E. Johns, I. Mudawar, An ultra-high power two-phase jet-impingement avionic clamshell module, J. Electron. Packag. 118 (1996) 264–270.
[7] I. Mudawar, D.E. Maddox, Enhancement of critical heat flux from high power microelectronic heat sources in a flow channel, J. Electron. Packag. 112 (1990) 241–248.
[8] C.O. Gersey, I. Mudawar, Effects of heater length and orientation on the trigger mechanism for near-saturated flow boiling critical heat flux—II. Critical heat flux model, Int. J. Heat Mass Transf. 38 (1995) 643–654.
[9] S. Mukherjee, I. Mudawar, Pumpless loop for narrow channel and micro-channel boiling, J. Electron. Packag. 125 (2003) 431–441.
[10] M.K. Sung, I. Mudawar, Single-phase and two-phase heat transfer characteristics of low temperature hybrid micro-channel/micro-jet impingement cooling module, Int. J. Heat Mass Transf. 51 (2008) 3882–3895.
[11] M.K. Sung, I. Mudawar, Single-phase and two-phase hybrid cooling schemes for high-heat-flux thermal management of defense electronics, J. Electron. Packag. 131 (2009) 021013.
[12] A. Berto, M. Azzolin, S. Bortolin, M. Miscevic, P. Lavieille, D. Del Col, Condensation heat transfer in microgravity conditions, Microgravity 9 (2023) 32.
[13] A. Berto, M. Azzolin, P. Lavieille, A. Glushchuk, P. Queeckers, S. Bortolin, C. S. Iorio, M. Miscevic, D. Del Col, Experimental investigation of liquid film thickness and heat transfer during condensation in microgravity, Int. J. Heat Mass Transf. 199 (2022) 123467.
[14] R. Raj, J. Kim, J. McQuillen, On the scaling of pool boiling heat flux with gravity and heater size, J. Heat Transf 134 (2012) 011502.
[15] T.R. Reinarts, F.R. Best, W.S. Hill, Definition of condensation two phase flow behaviors for spacecraft design, in: AIP Conf. Proc, AIP, 1992, pp. 1216–1225.
[16] I. Mudawar, S.J. Darges, M.M. Hasan, H.K. Nahra, R. Balasubramaniam, J. R. Mackey, Experimental investigation and analysis of flow condensation heat transfer in microgravity–Experiments onboard the International Space Station, Int. J. Heat Mass. Transf. 254 (2026) 127602.
[17] C.Y. Zhao, D. Qi, W.T. Ji, P.H. Jin, W.Q. Tao, A comprehensive review on computational studies of falling film hydrodynamics and heat transfer on the horizontal tube and tube bundle, Appl. Therm. Eng. 202 (2022) 117869.
[18] C.R. Kharangate, I. Mudawar, Review of computational studies on boiling and condensation, Int. J. Heat Mass Transf. 108 (2017) 1164–1196.
[19] I. Malgarinos, N. Nikolopoulos, M. Marengo, C. Antonini, M. Gavaises, VOF simulations of the contact angle dynamics during the drop spreading: standard models and a new wetting force model, Adv. Colloid Interface Sci. 212 (2014) 1–20.
[20] Y. Xue, C. Guo, X. Gu, Y. Xu, L. Xue, H. Lin, Study on flow characteristics of working medium in microchannel simulated by porous media model, Micromachines (Basel) 12 (2020) 18.
[21] J. Lee, L.E. O'Neill, I. Mudawar, 3-D computational investigation and experimental validation of effect of shear-lift on two-phase flow and heat transfer characteristics of highly subcooled flow boiling in vertical upflow, Int. J. Heat Mass Transf. 150 (2020) 119291.
[22] J. Lee, S. Kim, I. Mudawar, Assessment of computational method for highly subcooled flow boiling in a horizontal channel with one-sided heating and improvement of bubble dispersion, Int. J. Therm. Sci. 184 (2023) 107963.
[23] I. Mudawar, J. Lee, Experimental and computational investigation into hydrodynamic and heat transfer characteristics of subcooled flow boiling on the International Space Station, Int. J. Heat Mass Transf. 207 (2023) 124000.
[24] I. Mudawar, S. Kim, J. Lee, A coupled level-set and volume-of-fluid (CLSVOF) method for prediction of microgravity flow boiling with low inlet subcooling on the international space station, Int. J. Heat Mass Transf. 217 (2023) 124644.
[25] E.Da Riva, D. Del Col, Effect of gravity during condensation of R134a in a circular minichannel, Microgravity Sci. Tec. 23 (2011) 87–97.
[26] E.Da Riva, D. Del Col, Numerical simulation of laminar liquid film condensation in a horizontal circular minichannel, J. Heat Transf. 134 (2012) 051019.
[27] S. Chen, Z. Yang, Y. Duan, Y. Chen, D. Wu, Simulation of condensation flow in a rectangular microchannel, Chem. Eng. Process.: Process Intensif. 76 (2014) 60–69.
[28] G.D. Qiu, W.H. Cai, S.L. Li, Z.Y. Wu, Y.Q. Jiang, Y. Yao, Numerical simulation on forced convective condensation of steam upward flow in a vertical pipe, Adv. Mech. Eng. 6 (2014) 589250.
[29] H. Lee, C.R. Kharangate, N. Mascarenhas, I. Park, I. Mudawar, Experimental and computational investigation of vertical downflow condensation, Int. J. Heat Mass Transf. 85 (2015) 865–879.
[30] C.R. Kharangate, H. Lee, I. Park, I. Mudawar, Experimental and computational investigation of vertical upflow condensation in a circular tube, Int. J. Heat Mass Transf. 95 (2016) 249–263.
[31] W. Li, J. Zhang, P. Mi, J. Zhao, Z. Tao, P.R.N. Childs, T.I.-P. Shih, The effect of gravity on R410A condensing flow in horizontal circular tubes, Numer. Heat Transf. Part A Appl. 71 (2017) 327–340.
[32] P. Li, Z. Chen, J. Shi, Numerical study on the effects of gravity and surface tension on condensation process in square minichannel, Microgravity Sci. Tec. 30 (2018) 19–24.
[33] C. Wu, J. Li, Interfacial wave behavior and its effect on the flow and condensation heat transfer in a microtube, Int. J. Heat Mass Transf. 127 (2018) 41–54.
[34] P. Toninelli, S. Bortolin, M. Azzolin, D. Del Col, Visualization and numerical simulations of condensing flow in small diameter channels, Heat Transf. Eng. 40 (2019) 802–817.
[35] X. Gu, J. Wen, J. Tian, S. Wang, J. Tu, Numerical study on condensation annular flow of R1234ze(E) inside an inclined tube, Appl. Therm. Eng. 163 (2019) 114359.
[36] Y. Lei, I. Mudawar, Z. Chen, Computational and experimental investigation of condensation flow patterns and heat transfer in parallel rectangular micro-channels, Int. J. Heat Mass Transf. 149 (2020) 119158.
[37] Y. Qiu, H. Lee, C.R. Kharangate, Computational investigation of annular flow condensation in microgravity with two-phase inlet conditions, Int. Commun. Heat Mass Transf. 118 (2020) 104877.
[38] W. Tang, W. Li, W.J. Minkowycz, A numerical investigation of convective condensation in micro-fin tubes of different geometries, Numer. Heat Transf. Part A Appl. 78 (12) (2020) 697–705.
[39] Y.T. Lee, S. Hong, L.H. Chien, C.J. Lin, A.S. Yang, Heat transfer and pressure drop of film condensation in a horizontal minitube for HFO1234yf refrigerant, Appl. Energy 274 (2020) 115183.
[40] Y. Dai, S. Zhu, Y. Guo, S. Zou, Numerical study on condensation heat transfer of R290 inside a 4-mm-ID horizontal smooth tube, J. Braz. Soc. Mech. Sci. & Eng. 44 (2022) 2.
[41] F.L. He, W.F. Du, J.Y. Miao, H.X. Zhang, S.X. Liu, C. Liu, J.F. Zhao, Numerical investigation of the gravity effect on two-phase flow and heat transfer of neon condensation inside horizontal tubes, Appl. Therm. Eng. 233 (2023) 121162.
[42] I. Mudawar, V.S. Devahdhanush, S.J. Darges, M.M. Hasan, H.K. Nahra, R. Balasubramaniam, J.R. Mackey, Effects of heating configuration and operating parameters on heat transfer and interfacial physics of microgravity flow boiling

with subcooled inlet conditions – Experiments onboard the International Space Station, Int. J. Heat Mass Transf. 217 (2023) 124732.
[43] W.H. Lee, A pressure iteration scheme for two-phase flow modeling, in: Multi-phase transport: fundamentals, reactor safety, applications, 1, 1980, pp. 407–431.
[44] G.B. Wallis, One-dimensional two-phase flow, McGraw-Hill, New York, 1969.
[45] R.K. Shah, A.L. London, F.M. White, Laminar Flow Forced Convection in Ducts, J. Fluids Eng. 102 (1980) 256–257.
[46] S. Kim, J. Lee, I. Mudawar, J. Hartwig, Computational investigation of vertical upflow boiling of liquid nitrogen and effects of bubble collision dispersion force, Int. J. Heat Mass Transf. 203 (2023) 123780.
[47] T.H. Phan, C.N. Huang, C.R. Kharangate, Capturing interfacial phase change and flow physics during vertical downflow condensation, Int. J. Heat Mass Transf. 247 (2025) 127149.
[48] A. Basaran, A.C. Benim, A. Yurddas, Prediction of heat and fluid flow in microchannel condensation, E3S Web Conf. 128 (2019).
[49] J. Li, J.K. Narayanan, C.R. Kharangate, Experimental investigation of external flow condensation heat transfer in horizontal tube-in-tube configuration, Int. J. Heat Mass Transf. 245 (2025) 127044.
[50] A. Berto, P. Lavieille, M. Azzolin, S. Bortolin, M. Miscevic, D. Del Col, Film thickness, interfacial waviness and heat transfer during downflow condensation of R134a, Appl. Therm. Eng. 214 (2022) 118808.
[51] I. Mudawar, M.A. El-Masri, Momentum and Heat Transfer Across Freely-Falling Turbulent Liquid Films, Int. J. Multiphase Flow 12 (1986) 771–790.